Article

Sequential Scheelite Mineralization of Quartz–Scheelite Veins at the Sangdong W-Deposit: Microtextural and Geochemical Approach

Woohyun Choi [1], **Changyun Park** [2], **Yungoo Song** [1,*], **Chaewon Park** [1], **Ha Kim** [1] **and Chulgyoo Lee** [1]

1   Department of Earth System Sciences, Yonsei University, 50 Yonsei-ro, Seoul 120749, Korea;
    woohyun16@yonsei.ac.kr (W.C.); parkcw@yonsei.ac.kr (C.P.); kimha8965@yonsei.ac.kr (H.K.);
    chklee77@gmail.com (C.L.)
2   Korea Institute of Geoscience and Mineral Resources, 905 Yeongilman-daero, Pohang 37559, Korea;
    cypark@kigam.re.kr
*   Correspondence: yungoo@yonsei.ac.kr

check for updates

Abstract: The Sangdong W (tungsten)-deposit is known as one of the world's largest W-deposits, a magmatic–hydrothermal ore deposit including both skarn and hydrothermal alteration zones. The strata-bound characteristic of the deposit resulted in three major orebodies (hanging wall, main, footwall). The main ore mineral is a scheelite ($CaWO_4$)–powellite ($CaMoO_4$) solid solution. We examined the fluid evolution and scheelite formation process of the quartz–scheelite veins of the ore deposit, based on the microtextures and geochemical characteristics of the scheelite. After the initial magmatic–hydrothermal fluid release from the granitic body, prograde skarn is formed. In the later prograde stage, secondary fluid rises and precipitates stage I scheelite. Well-developed oscillatory zoning with the highest Mo content indicates continuous fluid infiltration under an open system. Pressure rises as mineralization occurs, generating the pressure release of the retrograde fluid. Fluid migrates downward by the gravitational backflow mechanism, forming stage II to IV scheelites. Dented oscillatory zoning of stage II scheelite is strong evidence of this pressure release. Stage III and IV scheelite do not show specific internal structures with pure scheelite composition. Retrograde scheelites are formed by fractional crystallization under a closed system. The observation of systematical fractional crystallization in the quartz–scheelite vein system is a meaningful result of our research. The geochemical characteristics and microtextural evidence imprinted in scheelites from each stage provide crucial evidence for the understanding of sequential scheelite mineralization of the quartz–scheelite vein system of the Sangdong W-deposit.

Keywords: Sangdong W-deposit; quartz–scheelite vein system; oscillatory zoning; systematical fractional crystallization

1. Introduction

The Sangdong W-deposit is a skarn to hydrothermal W–Mo–Bi deposit located in Taebaeksan mineralized district, in the eastern region of South Korea. As one of the largest W-deposits in the world, the Sangdong mine produced around 6Mt of scheelite raw ore every year from 1947 to 1992, until it ceased production [1]. Major biproducts of scheelite were bismuthinite (Bi_2S_3), molybdenite (MoS_2), and gold (Au) [1]. Recently, the Sangdong mine began to consider restarting W-production, willing to provide a reasonable amount of W to the global market.

The Sangdong W-deposit shows strata-bound scheelite mineralization in the limestone intercalation of Cambrian Myobong slate formation (Figure 1). Ore bodies of the Sangdong W-deposit consisted of a

hanging wall orebody (H1) at the upper boundary of Cambrian Myobong slate formation and Pungchon limestone formation, main orebody (M1) and footwall orebodies (F1, F2, F3, F4, ...) in the Myobong slate formation (Figure 1B). Early prograde skarn of the Sangdong W-deposit did not mineralize a meaningful grade of scheelite ores. The hydrothermal alteration stage and quartz veins formed high grade W–Mo ore bodies, with an average of 0.52% WO_3 [1,2]. It indicates that the vein system was the main scheelite formation process of the Sangdong W-deposit. The quartz–scheelite vein system of the Sangdong W-deposit was previously researched by fluid inclusion studies [3], which indicated the P–T conditions of vein formation. However, the scheelite of this quartz–scheelite vein system was not researched in detail, even though it is the major ore mineral of the deposit.

Scheelite ($CaWO_4$) is the most important W-ore mineral, mainly found in the hydrothermal vein-type W-deposits and skarn W–Mo deposits [4–6]. Due to its geochemical characteristics, scheelite forms a complete solid solution with powellite ($CaMoO_4$). Mo substitution of scheelite mainly depends on the oxygen (fO_2) and sulfur (fS_2) fugacity of the system, which changes dynamically as ore develops [7]. Additionally, scheelite holds a reasonable amount of trace elements substituted in the Ca site. Due to this characteristic, scheelite can act as a useful geochemical environment tracer of the ore deposit [8–12].

Recently, detailed studies about in situ trace element chemistry using laser ablation inductively coupled plasma mass spectrometry (LA-ICP-MS) and textural observations using cathodoluminescence (CL) images became common and useful tools to research scheelite. The REE (Rare earth element) geochemistry of scheelite was researched previously by many researchers, and they found that scheelite successfully inherits the REE characteristics of the parental ore forming fluid [8–13]. Fractional crystallization of REE is an important mechanism of scheelite mineralization, which affects the REE profile and Eu anomalies of scheelite [9]. In previous studies, this fractional crystallization was mostly observed in single grains which underwent several mineralization stages [9,13].

In this contribution, we used CL image observation and LA-ICP-MS trace element analysis to study the microtextures and geochemical behavior of scheelite from the quartz–scheelite vein system of Sangdong W-deposit. We could elucidate sequential scheelite mineralization and provide evidence of the systematical fractional crystallization of REE by scheelite in the quartz–scheelite vein system. By tracking the fluid evolution history of the deposit, we could suggest a modified scheelite mineralization model of the Sangdong W-deposit which could be helpful for the further exploration of the deposit.

2. Geological Settings

2.1. Regional Geology

The Sangdong W-deposit is located in the Taebaeksan mineralized district, the main mineral district of the mid-eastern Korean Peninsula (Figure 1A). It was formed at the margin of the Okcheon Belt and the Gyeonggi Massif. The basement strata consisted of Precambrian Gyeonggi (2.7–0.8 Ga) and Yeongnam Massifs (3.1–0.7 Ga) [13–15]. They are mainly formed with interbedded limestones, gneisses, phyllites, mica schists, and micaceous quartzites, with a general strike of N50°W and dip to 30°NE [14,16]. Weakly metamorphosed Paleozoic sedimentary rocks (Choseon and Pyeongan supergroup) overlying these basement strata form various metal deposits such as Cu–Fe–Au–W–Mo (Shinyemi deposit), Pb–Zn (Gagok deposit), Pb–Zn–Ag (Uljin deposit), Pb–Zn–Fe–W (Weondong deposit), and W–Mo–Bi (Sangdong deposit) [17,18]. Plutonic rocks described in this area are Daebo granites (Jurassic, 193–131 Ma), Bulgugsa granites (Cretaceous, 108–50 Ma), and regional small-scale intrusions [13,18–21]. Cretaceous Bulgugsa granite intrusion is known as the main heat source for the hydrothermal ore deposits of the area [18,22–25]. This originated at the epizone, with a low pressure of generally under 2.8 kbar [26,27].
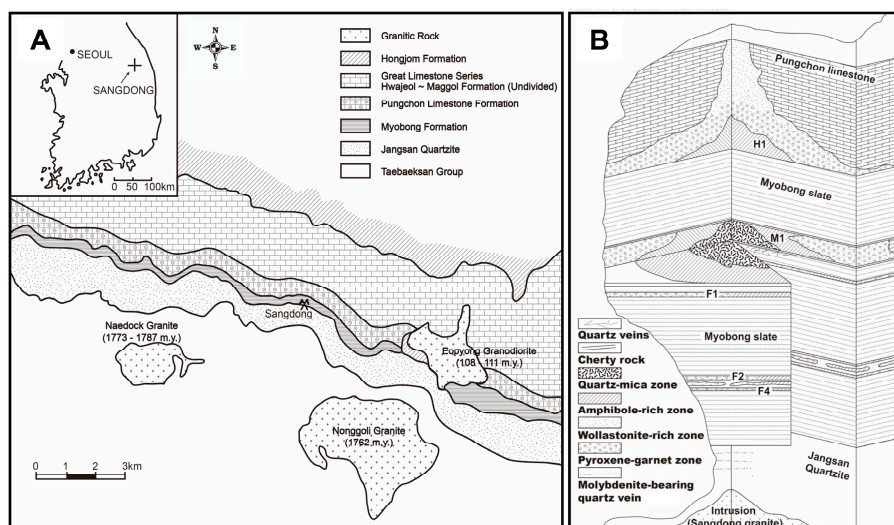
Figure 1. (**A**) Regional geologic map of the Sangdong W-deposit in the Taebaeksan mineralized district, including neighboring granitic bodies (modified from [16]). (**B**) Schematic cross-section of the Sangdong W-deposit including orebodies (modified from [28]; H: hanging wall orebody, M: main orebody, F: footwall orebody).

The Taebaeksan mineral district was defined as a granitic low-pressure hydrothermal ore system [18]. O and H stable isotope analysis was performed for the granitic intrusions to identify the fluid chemistry and the magma source. The O isotope resulted in a range of −14.0‰ to −8.7‰ (average −1.8‰) and the H isotope showed a range of −97.0‰ to −41.0‰ (average −70.0‰) [18]. Depletion of the oxygen isotope can be attributed to meteoric water infiltration during the cooling period of granitic intrusions [18]. Hydrogen isotope depletion can be attributed to gas release during the magma cooling process, which reveals that the hydrothermal fluids that triggered ore formation came from highly evolved melt [29]. This strongly indicates that the ore forming fluid of the Taebaeksan mineral district was a mixture of magmatic fluid from granitic intrusions and meteoric water infiltration from the shallow surface [13,18,30].

2.2. Deposit Geology

The Sangdong tungsten deposit is located in the southern area of the Taebaeksan mineral district. It is one of the largest W-deposits in the world, with an estimated ore reserve of more than 60,000 metric tons of tungsten minerals [15,28]. Its location is around 37°8'7" N and 128° 50'3" E (Figure 1A).

The main host formations of the Sangdong deposit are the Myobong slate formation (80–150 m thickness) and the Pungchon limestone formation (1150–1470 m thickness) [16] (Figure 1B). The Myobong formation (Cambro-Ordovician Choseon supergroup) mainly consists of phyllite, black slate, and shale, with limestone intercalation of various thicknesses, ranging from 0.3 to 20 m [16,28]. The main orebody (M1) and footwall orebodies (F1–F4) with high productivity of tungsten are located at this Myobong slate formation. Jangsan quartzite (150–200 m thickness) appears below the Myobong slate formation. Only quartz–molybdenite veins (no scheelite content) are observed in this quartzite formation [28]. Pungchon limestone formation (Cambro-Ordovician Choseon supergroup) conformably overlies the Myobong slate formation, consisting of massive limestone, thin shale interbeds, and weakly altered metamorphic rocks [16,28]. The hanging wall orebody (H1), with a relatively higher molybdenum content, appears in the lower strata of the formation. Above these Cambro-Ordovician formations, Carboniferous Hongjom formation (250–350 m thickness) overlies, with shale, sandstone, conglomerate, and cherty lithologies [16,28].

Igneous intrusions found near the Sangdong deposit are Precambrian Naedock (1780 Ma) and Nonggori (1762 Ma) granites at the south-east and Cretaceous Eopyong granodiorite (110 Ma) at the west [16,28]. The radiometric age of the deposit (86.6 to 87.2 Ma) indicates that neighboring

granitic intrusions did not affect the ore formation of Sangdong deposit [3]. Hidden Sangdong granite (87.5 Ma) was not found during the surface exploration but appeared beneath Jangsan quartzite during the drilling exploration [31]. This age provides a good match with the ore formation timing. The Sangdong granite is mainly composed of quartz, K-feldspar, plagioclase, and muscovite (partial chlorite alteration was observed), with calcite, magnetite, and apatite as accessory minerals [16,31]. It includes quartz veins, potassic and pyritic alteration with trace amounts of scheelite, bismuthinite, and molybdenite [16,31].

The orebodies of the Sangdong deposit were mainly controlled by lithological conditions, which resulted in its strata-bound nature, showing similar strike and dip to their host formations [16,28]. The major orebodies can be classified into a primary mineralization zone (early dry skarn) and a late hydrothermal mineralization zone (vein formation) [2,32,33]. The skarn zones mainly present anhydrous skarn minerals such as garnet (grossular-andradite) and clinopyroxene (diopside-hedenbergite) at the outer rim of the deposit, whereas quartz vein dominated zones show overprints of altered hydrous minerals such as muscovite, biotite, and amphibole [3,15,28].

The primary mineralization zone is the early stage pyroxene-garnet skarn which forms the outer rim of the deposit. The tungsten content is relatively lower (0.25% to 0.5% WO_3) than the hydrothermal mineralization zone [28]. This dry skarn stage can be classified into garnet–wollastonite skarn and pyroxene–garnet skarn [28,34]. The garnet–wollastonite skarn constitutes the outermost part of the dry skarn with low (<0.1% WO_3) tungsten content [28]. The main ore forming minerals are pyroxene (diopside), garnet, calcite, and wollastonite, with scarce sulfide and iron oxide minerals [28]. The pyroxene–garnet skarn is surrounded by the garnet–wollastonite skarn, also with low (<0.3% WO_3) tungsten content [28]. The main mineral assemblages of the skarn are pyroxene (hedenbergite), garnet (grossular-andradite), quartz, calcite, chlorite, fluorite, amphibole, pyrrhotite, native bismuth, and scheelite [28]. Different types of pyroxenes are a major characteristic by which to divide each skarn zone. These mineral assemblages of the primary mineralization zones show that they originated from the prograde skarn formation process.

The late hydrothermal mineralization zone is the inner core part of the deposit, which formed after the skarn forming processes [28]. The tungsten content is relatively higher (0.5% to 3.0% WO_3) than the prograde skarn zones [28]. This zone can be divided into a quartz–mica core and an amphibole-rich rim [28,34]. The amphibole-rich zone is mostly composed of amphibole (Fe-hornblende), chlorite, scheelite, and quartz, with minor fluorite, pyrite, pyrrhotite, fluorite, apatite, and bismuthinite [28]. Scheelite mainly occurs along micro fractures and quartz veins at the amphibole schists. The quartz–mica zone constitutes the innermost core part of the deposit with the highest (1.5% to 3.0% WO_3) tungsten content [28]. Biotite, chlorite, quartz, and scheelite are the most common minerals, with minor apatite, calcite, fluorite, and muscovite. Quartz veins appear more frequently at the quartz–mica zone, commonly containing a scheelite and chlorite filling. The upper and lower margins of the main and footwall orebodies are buried with cherty rock composed of Ca-plagioclase and fine amphibole veinlets [3].

3. Analytical Methods

3.1. Sample Preparation

Samples were collected from the hanging wall orebody (S1 and S2), main orebody (S3), and footwall orebody (S4) of the Sangdong mine. Samples from the hanging wall orebody displayed light green to blue fluorescence under UV lamp light. Main and footwall orebody samples showed only blue fluorescence color under UV lamp light. Collected samples were classified and processed into thin sections and rock slabs. All the thin sections and slabs were polished until diamond (1 μm) mesh and carbon-coated for CL and electron probe micro analyzer (EPMA) observation.

3.2. SEM-BSE-CL Image Observation

Backscattered electron images (BSE) and CL images of the carbon-coated thin sections were obtained from a high vacuum (HV) scanning electron microscope (SEM; JSM-6610LV) at the Korea Basic Science institute (KBSI) campus in Ochang, Korea. SEM was operated at 10 Pa pressure, with a 15 kV accelerating voltage. The attached BSE detector was model 51-ADD0021 INCA x-act from Oxford instrument. The CL detector was the Mini CL from Gatan.

3.3. EPMA-WDX Point Analysis

Major element analysis of scheelite and chlorite was performed using an EPMA (JXA-8100) with a wave dispersive X-ray (WDX) mode at Yonsei University, Seoul, Korea. Performance conditions were 20 kV accelerating voltage and a 5 µm probe diameter with 20 nA probe current. Used standards were almandine (Al, and Fe), Cr-diopside (Si, Ca, and Mg), rhodonite (Mn), sanidine (K), albite (Na), rutile (Ti), molybdenite (Mo), and metal tungsten for W.

3.4. LA-ICP-MS Point Analysis

REE and trace element analysis were performed using LA-ICP-MS (Analyte Excite; 193 nm; TELEDYNE CETAC) at the KBSI Ochang campus, Korea. The laser repetition rate was 10 Hz, with a 5 J/cm^2 energy density, 10 ms dwell time, 15 µm/s scan speed, and 30 µm spot size. Ca was chosen for the internal standard and a NIST 612 glass for the external standard [35]. Data reduction was done by using Glitter software, developed by the ARC National Key Centre for Geochemical Evolution and Metallogeny of Continents (GEMOC) and CSIRO Exploration and Mining. Analyzed elements were Na (23), Ti (48), Fe (57), Rb (85), Sr (88), Y (89), Zr (90), Nb (93), Mo (95), La (139), Ce (140), Pr (141), Nd (146), Sm (147), Eu (153), Gd (157), Tb (159), Dy (163), Ho (165), Er (166), Tm (169), Yb (172), Lu (175), Hf (178), Ta (181), Pb (208), Bi (209), Th (232), and U (238).

4. Results

4.1. Paragenesis of the Deposit

The paragenesis pattern of the deposit can provide useful information about ore forming processes and fluid migration. Major minerals of the vein-type scheelite ore are scheelite, fluorite, quartz, apatite, and chlorite. Just a small number of studies have described the mineral occurrence of the Sangdong W-deposit previously [3,24,28]. Based on our samples, we could classify the paragenesis of the deposit into four stages (Figure 2). Stage I is quartz–scheelite ± fluorite ± apatite. No sulfide minerals were observed at this stage. Stage II is scheelite–chlorite–fluorite ± calcite ± quartz ± pyrrhotite. Scheelite is dominant at the vein structure and chlorite starts to appear. Stage III is quartz–scheelite–ferro-actionolite ± pyrrhotite ± bismuthinite ± chlorite ± biotite ± fluorite ± apatite ± native bismuth. Abundant bismuthinite and the existence of native bismuth are unique characteristics of stage III. Stage IV is quartz–stilbite–chlorite–scheelite ± fluorite ± apatite ± pyrite ± sphalerite ± bismuthinite. Authigenic chlorite is well observed along the vein edge. Descriptions of each stage are reported below.

4.1.1. Quartz–Scheelite ± Fluorite ± Apatite (Stage I)

Stage I minerals represent the quartz–scheelite vein formed during the late prograde stage (Figure 3). Dominant minerals observed in the vein are quartz and scheelite, with minor fluorite and apatite. Fluorite and apatite appear both as inclusions and as independent grains in the veins. Secondary minerals such as biotite, muscovite, K-feldspar, and Ca-plagioclase surround the quartz–scheelite vein, but no sulfide minerals can be observed. The absence of hydrated minerals and sulfide minerals in the veins are powerful evidence of the prograde stage origin of this stage I scheelite at the hanging wall orebody [36].

Stage / Mineral	Stage I	Stage II	Stage III	Stage IV
	Hanging wall orebody Quartz vein	Hanging wall orebody Scheelite Vein	Main orebody Quartz Vein	Footwall orebody Quartz Vein
Quartz				
Scheelite				
Fluorite				
Apatite				
Bismuthinite				
Bismuth				
Pyrrhotite				
Pyrite				
Ferro-actinolite				
Chlorite				
Calcite				
Muscovite				
Sphalerite				
Biotite				
Stilbite				

Figure 2. Schematic diagram of mineral paragenesis of Sangdong W-deposit. Bold lines show major paragenetic minerals of the veins, solid lines are minor minerals of each stage, and dashed lines are accessory minerals.
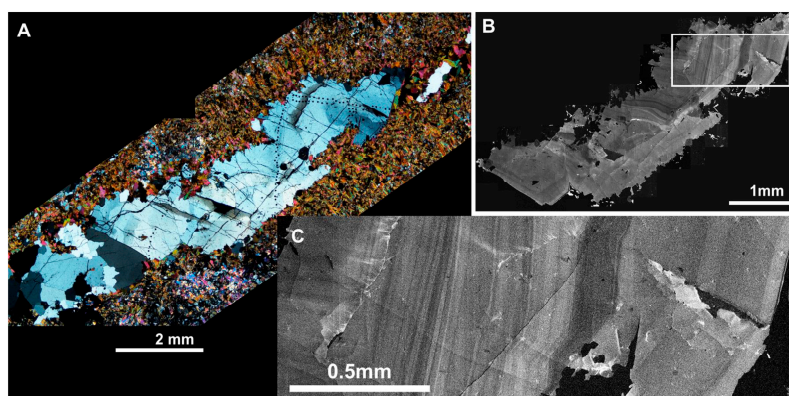

Figure 3. Optic and SEM image of stage I scheelite. (**A**) Polarized microscope image of stage I scheelite. Scheelite grain is large and fills vein space by itself. Outer margin of scheelite grain is dissolved and filled with secondary biotite and muscovite. (**B**) Cathodoluminescence (CL) image of stage I scheelite in small magnification. Oscillatory zoned core parts and relatively bright rim part are easily distinguishable. (**C**) CL image of stage I scheelite with larger magnification. Thickness of oscillatory zones becomes wider in the direction of the rim; contrast also becomes brighter in the same direction.

The scheelite in stage I is composed of large-grained (up to 5 mm) subhedral crystals, with clear oscillatory zoning detected under BSE and CL (Figure 3B, C). They grew enough to fill the whole vein structure, with no later stage authigenic chlorite like stage III and IV (Figure 3A). Extra vein spaces are filled with quartz grains with clear internal textures. Fluorite and apatite are generally included in the scheelite grains, indicating that they were formed earlier than scheelite. The sharp boundary between the scheelite and quartz clusters indicates that they were formed contemporarily Scheelite at this stage shows both green and blue fluorescence under UV lamp light.

4.1.2. Scheelite–Chlorite–Fluorite ± Calcite ± Quartz (Stage II)

Stage II minerals represent scheelite veins formed at the early retrograde stage (Figure 4A–D). The principal mineral assemblage of this stage is scheelite, chlorite, and fluorite, with minor calcite, quartz, and pyrrhotite. Ferro-actinolite, Ca-plagioclase, and stilbite are found as secondary minerals. Ferro-actinolite grains were large and massive, showing alteration into chlorite. Stilbite veins crosscut secondary ferro-actinolite and scheelite grains, suggesting that they were formed later than the scheelite veins at stage II. The appearance of hydrous minerals (i.e., ferro-actinolite and chlorite) and the existence of accessory sulfide minerals with relatively low sulfur content (i.e., pyrrhotite) indicate that stage II veins were formed at the early retrograde stage (36).
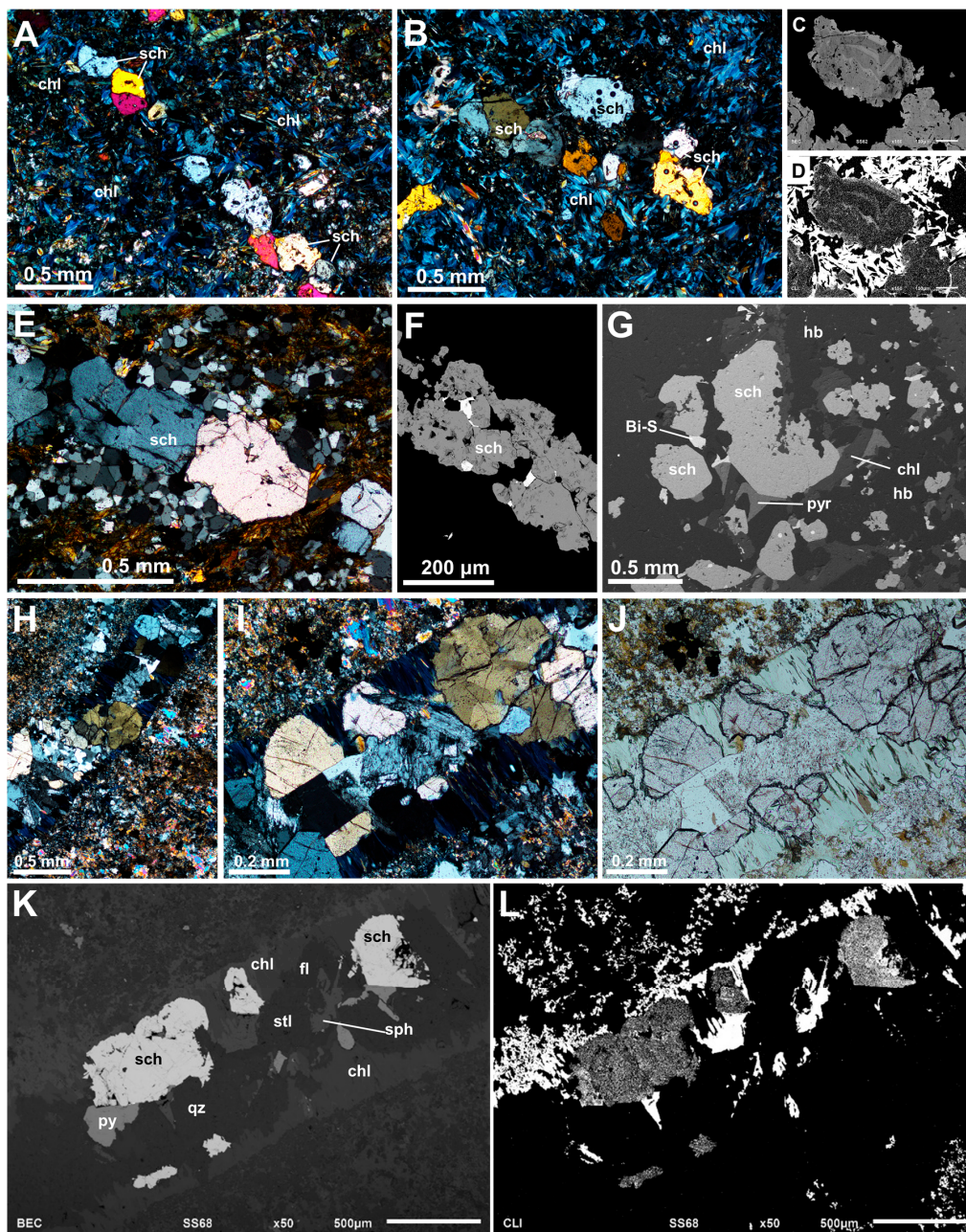
Figure 4. Optic and SEM images of stage II, III, and IV scheelites. (**A**–**D**) Stage II scheelite shows scheelite-dominated vein structure. Secondary chlorite alteration is well observed throughout overall section. Oscillatory zoning with dented zones is commonly observed. Scheelite grains are mid-sized subhedral to anhedral grains; rim parts have overgrowth of pure scheelite with brighter CL. (**E**–**G**) Stage III scheelite shows scheelite-dominated vein structure but quartz is more abundant than stage II scheelite. Scheelite grains are relatively smaller than stage II scheelite, with anhedral to subhedral shape and elongation along the vein. No specific internal structures are shown in CL or BSE images. Native bismuth commonly exists as inclusions; bismuthinite and pyrrhotite appear as dominant sulfide phase. (**H**–**L**) Stage IV scheelite shows quartz-dominated vein structure, showing later stilbite alteration. Scheelites have smallest size and are disseminated along the veins. Grain boundaries are commonly dissolved and secondary chlorites grow with saw-blade shape along the vein margins. No specific internal structures are visible in the scheelite grains. Pyrite appears as dominant sulfide phase with minor sphalerite. Chl: chlorite, Sch: scheelite, Hb: hornblende, Pyr: pyrrhotite, Bi-S: bismuth sulfide, Fl: fluorite, Py: pyrite, Sph: sphalerite, Qz: quartz, Stl: Stilbite.

Stage II scheelites are smaller than stage I scheelite but still constitute a dominant phase of the vein system (Figure 4A,B). They are medium-grained (up to 0.5 mm) subhedral and anhedral crystals with dented oscillatory zonings and also patchy zoning (Figure 4C,D). Zones were narrower than stage I scheelite and did not show a clear contrast difference. Few grains had fluorite and apatite inclusions, but fluorite more commonly existed along the veins. Outer boundaries of the scheelite grains are dissolved and replaced with authigenic chlorites, suggesting that chlorites were formed after scheelite formation. Scheelite of this stage also shows both green and blue fluorescence under UV lamp light.

4.1.3. Quartz–Scheelite–Ferro-Actinolite ± Pyrrhotite ± Bismuthinite ± Chlorite ± Biotite ± Fluorite ± Apatite ± Native Bismuth (Stage III)

Stage III minerals consist of quartz–scheelite veins formed at the retrograde stage (Figure 4E–G). Dominant mineral phases are quartz, scheelite, and ferro-actinolite, with relatively minor amounts of chlorite, biotite, fluorite, apatite, and sulfide minerals (i.e., bismuthinite, pyrrhotite). A unique characteristic of this stage is the abundant bismuth minerals (Figure 4F,G). Bismuthinite exists with a pore-filling texture and native bismuth occurs as inclusions inside scheelite grains. This reveals that bismuth was precipitated before scheelite mineralization and switched into bismuthinite after scheelite mineralization as the sulfur fugacity of the system increases. The mineral assemblage of stage III shows the typical mineral distribution of a main (middle) orebody with quartz–amphibole alteration [3]. Evidence of hydrous minerals and abundant sulfide minerals suggest that scheelite of stage III was formed during the retrograde process [36].

Stage III scheelites are relatively larger and longer than stage II scheelites (up to 1.5 mm), showing subhedral to anhedral form. Grains commonly grew along the veins and appear as elongated forms (Figure 4F). Scheelite grains have apatite and native bismuth as inclusions. Neither BSE nor CL images showed significant internal zoning textures. Grain boundaries generally show dissolution textures and an overprint of chlorite and sulfide minerals (Figure 4G). Scheelite of this stage shows bright blue fluorescence under UV lamp light.

4.1.4. Quartz–Stilbite–Chlorite–Scheelite ± Fluorite ± Apatite ± Pyrite ± Sphalerite ± Bismuthinite (Stage IV)

Stage IV consists of altered quartz–scheelite veins formed at the latest retrograde stage (Figure 4H–L). The predominant mineral phases are quartz, stilbite, chlorite, and scheelite, with minor amounts of fluorite, apatite, and sulfide minerals (i.e., pyrite, sphalerite, bismuthinite). The existence of stilbite and abundant fluorite indicates the calcium-rich condition of the fluid. Sulfide minerals mainly consist of pyrite and sphalerite, with a minor amount of bismuthinite (Figure 4K). Sawblade-shaped authigenic chlorites grew along the vein boundaries. Abundant hydrous minerals and sulfide minerals with high sulfur content (i.e., pyrite, sphalerite) are strong evidence of the retrograde process [36].

Stage IV scheelites are fine-grained (up to 0.5 mm) and show subhedral to anhedral crystal shapes (Figure 4H–L). BSE and CL images do not show meaningful contrast differences or zoning patterns. Some grains show diamond-shaped growth boundaries between internal crystals in CL images but do not show significant differences (Figure 4L). Scheelite grains are disseminated along the quartz veins and show dissolution textures at the boundaries with chlorites. Scheelite at this stage shows bright blue fluorescence under UV lamp light.

4.2. Scheelite Microtexture

Microtextures of scheelite from the Sangdong W-deposit are displayed in Figures 3 and 4. The main texture of stage I scheelite is oscillatory zoning (Figure 3B,C). Zones show a wide range of thicknesses (from 10 to 200 μm), with a consistent direction of crystal planes (Figure 3B,C). Zone thickness differs with direction but generally becomes wider when approaching the rim. The upper core part of the zoning shows darker contrast in the BSE and CL images, indicating higher Mo content than the bright areas of the rim (Figure 3B,C). At the middle part of the oscillatory zoning, the thick zone with dark

contrast shows discontinuity. Dissolved margins and biotite filling indicate mica alteration at a later stage (Figure 3B,C). Most areas of the rim show dissolution textures but contact with quartz grains at the left is sharp and clear. Fluorites and apatites are found as inclusions inside scheelite grains.

The main texture of stage II scheelite is also oscillatory zoning combined with overgrowth rims (Figure 4A–D). As scheelite grains are smaller than stage I scheelites, zone thicknesses are much thinner (up to 20 μm), with dented shapes. Oscillatory zoning does not show the shape of the scheelite crystal planes as stage I scheelites. Scheelites with relatively bright contrasts show overgrowth around dark areas, suggesting a different stage of precipitation (Figure 4C,D). This rim overgrowth commonly shows dissolution textures and is associated with later stage chlorites. Fluorite and apatite were the main inclusion minerals, with a minor amount of quartz.

Stage III scheelite does not show any internal zoning textures in the BSE and CL images (Figure 4F,G). Scheelite grains are elongated along the vein directions as subhedral or anhedral grain shapes. Minor amounts of relatively small-sized scheelite grains show euhedral shapes. Native bismuth is well observed as inclusions with minor fluorite and apatite (Figure 4F,G). Grain boundaries are commonly dissolved and filled with authigenic chlorites.

Stage IV scheelites also do not show any meaningful internal zoning textures in either the BSE or CL images (Figure 4K,L). Scheelite grains are smaller than other stages, disseminated along the vein edges. Grain boundaries are commonly dissolved and replaced with authigenic chlorites. Margins between scheelite and quartz grains are commonly sharp and straight, showing that they were formed simultaneously (Figure 4H–L). Fluorites are mostly found along quartz grains, but some exist as inclusions inside scheelite grains.

4.3. Major and Trace Element Composition of Scheelite

Major element EPMA analyses were conducted for Na_2O, CaO, MoO_3, and WO_3 (Table 1 and Supplementary Table S1). The WO_3 and MoO_3 content of stage I scheelite differed along the oscillatory zoning. Core parts with darker contrast show the highest MoO_3 content (2.26 wt.%) and lowest WO_3 content (76.61 wt.%). Approaching the bright area of the rim, WO_3 content increases (79.91 wt.%) and MoO_3 content decreases (0.00 wt.%). Each oscillatory zone showed different W–Mo content. This reflects well the solid solution of the scheelite–powellite series, showing that grains with darker contrasts have higher Mo content. Stage II scheelite also shows a difference in Mo content according to contrast (Table 1).

Table 1. Major element analysis data of Sangdong scheelites (in brief) *.

Stage	Stage I (*n* = 145) **			Stage II (*n* = 50)			Stage III (*n* = 20)			Stage IV (*n* = 50)		
	Max	Min	Average	Max	Min	Average	Max	Min	Average	Max	Min	Average
Oxide composition (wt%)												
CaO	21.38	20.68	20.97	21.56	20.45	21.08	21.11	21.21	20.83	19.81	19.67	19.72
MoO_3	2.26	0.00	0.79	0.36	0.06	0.20	0.22	0.00	0.13	0.17	0.00	0.04
WO_3	76.61	79.09	78.06	77.36	79.53	78.50	78.75	79.13	79.03	80.28	80.29	80.03
Na_2O	0.03	0.05	0.06	0.00	0.00	0.03	0.05	0.00	0.03	0.00	0.04	0.02
Total	100.27	99.82	99.87	99.28	100.04	99.82	100.13	100.34	100.03	100.26	100.00	99.81
Number of ions based on 4 oxygen												
Ca	1.07	1.06	1.07	1.10	1.05	1.08	1.07	1.08	1.06	1.01	1.01	1.01
Mo	0.04	0.00	0.02	0.01	0.00	0.00	0.00	0.00	0.00	0.00	0.00	0.00
W	0.93	0.98	0.96	0.96	0.98	0.97	0.97	0.97	0.98	0.99	1.00	0.99
Na	0.00	0.00	0.00	0.00	0.00	0.00	0.00	0.00	0.00	0.00	0.00	0.00
O	4.00	4.00	4.00	4.00	4.00	4.00	4.00	4.00	4.00	4.00	4.00	4.00
Scheelite endmember mole fraction												
Sch	0.93	0.98	0.96	0.96	0.98	0.97	0.97	0.97	0.98	0.99	1.00	0.99
Po	0.04	0.00	0.02	0.01	0.00	0.00	0.00	0.00	0.00	0.00	0.00	0.00

* Detailed data are provided in Supplementary Table S1; ** Numbers inside parentheses are total numbers of point analyses for each sample.

Overall Mo content decreased from stage I scheelite (0.06 to 0.36 wt.%). Stage III (0.00 to 0.22 wt.%) and stage IV (0.00 to 0.17 wt.%) scheelites had lower Mo content than stage I and stage II scheelites. BSE images of stage III and IV scheelites did not show meaningful contrast changes across the grains, and this fits well with the almost pure scheelite composition. The CaO composition was uniform at each stage, at around 20.0 wt.% (Table 1). All the EPMA analysis data of scheelite are provided in Table S1.

REE point analysis showed meaningful changes throughout the stages (Figure 5 and Table 2). Stage I scheelite shows two distinct REE patterns (Figure 5A). The oscillatory zoned parts of stage I scheelite (S1-O of Figure 5A) have a positively inclined LREE-enriched pattern with negative Eu anomaly. Light rare earth elements (LREE; La to Sm) range from 54.6 to 746.6 ppm and heavy rare earth elements (HREE; Ho to Lu) range from 1.223 to 63.11 ppm (Figure 5A and Table S2). The REE pattern scatters along the different oscillatory zones, but the overall shape remains uniform. The outer area of the rim of stage I scheelite (S1-R of Figure 5A) has an LREE-depleted M-type tetrad pattern with negative Eu anomaly. LREE ranges from 13.4 to 196.91 ppm and HREE ranges from 3.84 to 128.51 ppm (Figure 5A and Table S2).
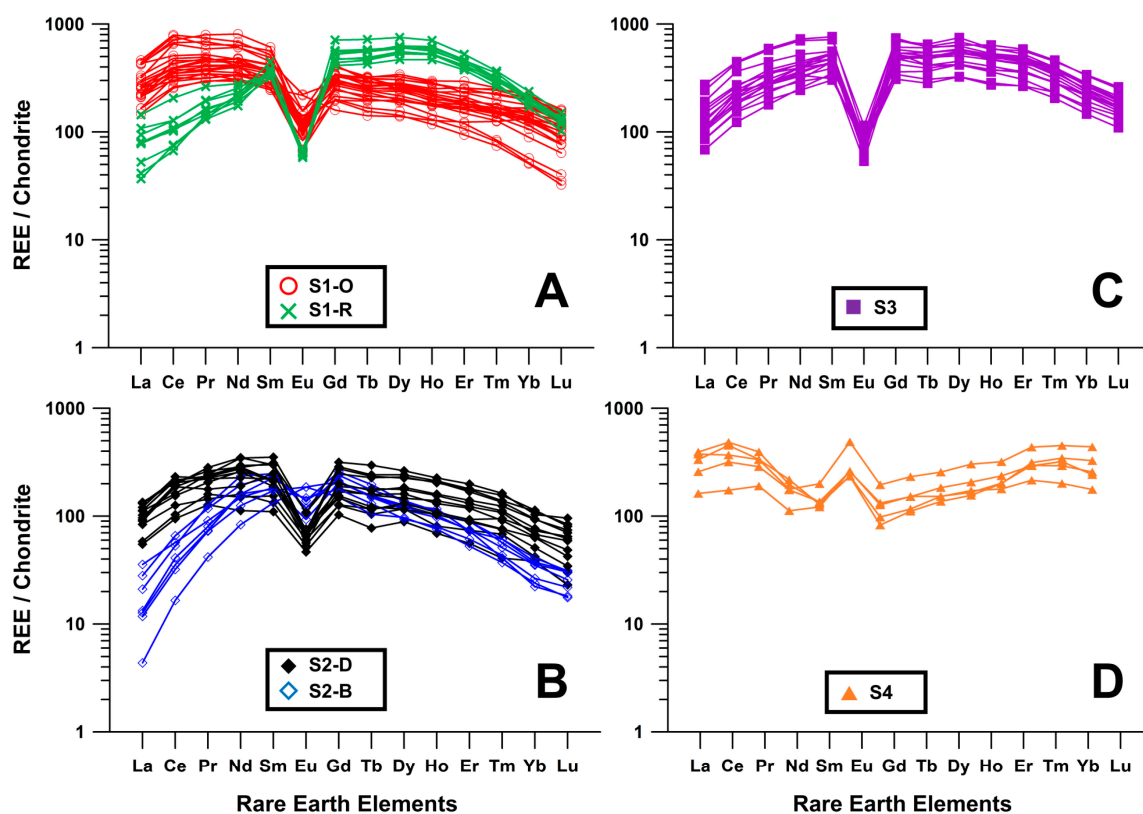

Figure 5. Chondrite normalized rare earth element (REE) profile of scheelite (chondrite data based on Taylor and McClennan (1985)). (**A**) Oscillatory zoned part of stage I scheelite (S1-O) shows positively inclined light REE (LREE)-enriched pattern with negative Eu anomaly. Rim area of stage I scheelite (S1-R) shows LREE-depleted and middle REE (MREE)-enriched pattern with negative Eu anomaly. (**B**) Dark CL area of stage II scheelite (S2-D) shows MREE-enriched pattern with negative Eu anomaly. Bright CL area of stage II scheelite (S2-B) shows LREE-depleted and MREE-enriched pattern with slightly negative or no Eu anomaly. (**C**) Stage III scheelite shows MREE-enriched M-type tetrad pattern with negative Eu anomaly. (**D**) Stage IV scheelite shows MREE-depleted pattern with W-type tetrad pattern with positive Eu anomaly.

Table 2. Trace element and REE analysis data of Sangdong scheelites (in brief) *.

Stage	Stage I (*n* = 32)			Stage II (*n* = 20)			Stage III (*n* = 20)			Stage IV (*n* = 5)		
	Max	Min	Average	Max	Min	Average	Max	Min	Average	Max	Min	Average
Na23	269.77	74.52	149.06	426.77	20.53	132.17	173.26	24.22	80.88	18,389.78	13,489.79	15,191.17
Ti48	94.84	61.68	71.40	106.10	60.06	83.95	70.14	58.71	65.59	90.39	68.86	78.35
Fe57	544.50	30.97	75.34	117.18	bdl	62.76	279.86	bdl	51.91	200.80	131.78	150.11
Rb85	5.15	bdl	0.28	0.46	bdl	0.09	bdl	bdl	bdl	5.32	3.82	4.27
Sr88	90.64	30.67	54.82	108.24	28.34	55.31	38.71	30.12	33.76	76.55	57.47	64.77
Y89	867.41	242.98	542.39	380.87	115.94	229.56	1192.47	613.31	901.63	691.14	472.45	562.81
Zr90	0.09	bdl	0.00	bdl	bdl	bdl	bdl	bdl	bdl	32.20	19.75	25.06
Nb93	479.81	59.53	234.94	353.79	10.14	148.67	183.63	64.17	114.82	184.77	14.11	51.57
Mo95	19,663.54	133.00	6783.24	47,891.12	459.96	21,199.52	811.75	219.83	567.98	179.17	134.40	160.22
La139	167.00	13.40	81.57	49.49	1.60	26.60	100.88	25.15	48.80	191.25	94.92	138.14
Ce140	746.60	63.34	331.46	222.58	15.85	123.80	429.51	117.98	225.44	506.03	304.07	411.87
Pr141	107.18	17.73	51.19	38.77	5.72	23.05	81.21	24.53	43.83	54.06	39.43	45.00
Nd146	566.83	122.40	272.31	248.20	59.27	152.95	516.36	147.75	280.20	154.89	102.42	129.55
Sm147	138.86	55.95	84.03	81.48	25.41	50.06	176.44	59.50	106.58	46.21	19.25	31.52
Eu153	19.14	5.00	9.02	16.19	4.05	8.42	10.01	4.68	7.10	42.54	20.35	27.48
Gd157	214.47	48.23	107.20	96.72	31.55	60.75	226.92	94.41	155.50	59.83	25.29	36.39
Tb159	41.17	8.10	18.77	17.20	4.50	9.47	37.70	16.44	27.59	13.46	4.77	8.05
Dy163	282.27	52.30	126.34	100.30	33.88	57.92	284.89	123.41	197.60	97.64	45.68	64.79
Ho165	59.13	9.93	25.59	19.26	5.90	11.02	54.28	23.29	39.27	25.81	9.70	16.11
Er166	128.51	23.08	62.30	49.51	13.13	26.80	145.61	66.19	106.67	79.74	35.06	54.75
Tm169	12.87	2.62	7.16	5.80	1.32	3.09	16.46	7.34	12.05	15.57	8.33	11.21
Yb172	58.05	12.44	38.04	28.15	5.53	15.07	83.80	36.41	60.24	112.20	72.68	84.55
Lu175	6.10	1.22	4.08	3.65	0.67	1.80	9.96	4.18	6.89	16.71	9.23	11.69
Hf178	0.42	0.08	0.20	0.20	bdl	0.08	0.40	0.20	0.30	0.86	0.64	0.74
Ta181	8.69	0.80	2.60	2.75	0.08	0.90	2.19	1.13	1.63	1.85	0.16	0.58
Pb208	3.76	1.33	2.42	3.06	1.41	2.18	2.37	1.45	1.78	4.27	2.71	3.44
Bi209	2.18	bdl	0.14	0.46	0.06	0.23	0.10	0.02	0.05	0.18	0.09	0.13
Th232	2.82	0.89	1.79	2.94	1.11	1.59	1.51	0.84	1.07	2.70	1.46	1.94
U238	1.69	0.07	0.42	0.56	0.04	0.20	0.18	0.06	0.11	0.89	0.31	0.58

* Detailed data are provided in Supplementary Table S2.

Stage II scheelite also shows two different REE patterns (Figure 5B). Scheelites with bright contrast (S2-B of Figure 5B) have a middle rare earth element (MREE; Eu to Dy)-enriched pattern with slight negative or no Eu anomaly. LREE differs from 1.6 to 167.61 ppm, MREE ranges from 7.57 to 79.04 ppm, and HREE ranges from 0.67 to 22.34 ppm (Figure 5B and Table S2). Scheelites with dark contrast (S2-D of Figure 5B) have MREE-enriched M-type tetrad patterns with negative Eu anomaly. LREE ranges from 17.48 to 245.64 ppm, MREE ranges from 4.05 to 100.3 ppm, and HREE ranges from 1.45 to 44.64 ppm (Figure 5B and Table S2). Comparing two fragments, LREE show significant depletion at the S2-B. Stage III scheelites have a uniform MREE-enriched M-type tetrad pattern with negative Eu anomaly (Figure 5C). The REE pattern did not change along the scheelite grains. LREE ranges from 24.53 to 516.36 ppm, MREE ranges from 4.68 to 284.89 ppm, and HREE ranges from 4.18 to 145.61 ppm (Figure 5C and Table S2). Stage IV scheelite has a uniform MREE-depleted W-type tetrad pattern with positive Eu anomaly (Figure 5D). LREE ranges from 83.33 to 528.77 ppm, MREE ranges from 82.24 to 488.97 ppm, and HREE ranges from 113.98 to 452.42 ppm (Figure 5D and Table S2). Slight REE concentration and MREE depletion with Eu anomaly change were observed from stage II to IV scheelites. Detailed analysis data are provided in Supplementary Table S2.

4.4. Major Element Composition of Associated Chlorite

Due to its geochemical characteristics, chlorite's composition has a close relationship with its formation temperature. This led to the formation of the chlorite geothermometer, which can be used in wide variety of geological conditions [37–43]. The first suggested chlorite geothermometric equation was a function of Al in the tetrahedral site of chlorite for hydrothermal environments [39]. This model was modified later, including Fe/(Fe + Mg) values as another factor [38]. We used this modified

model to calculate the chlorite formation temperature of the Sangdong W-deposit. The equation of the geothermometer is as follows:

$$Al_c^{IV} = Al^{IV} + 0.7 \left[\frac{Fe}{Fe + Mg} \right] \tag{1}$$

$$T \; (°C) = 106 \; Al_c^{IV} + 18 \tag{2}$$

The calculated temperatures and EPMA data of each stage are provided in Table 3 and Figure 6. According to the classification system, chlorites of the Sangdong W-deposit are mostly brunsvigite ($2.75 \leq Si_T \leq 3.1$, $0.25 \leq Fe/(Fe + Mg) \leq 0.75$), a relatively Fe-rich chlorite. Chlorite appears from stage II to VI, showing no occurrence in stage I veins. The stage II chlorite temperature varies from 145.1 to 177.0 °C (average 166.7 ± 6.75 °C), showing the lowest temperature. Stage III chlorite's temperature varies from 169.9 to 196.9 °C (average 183.2 ± 8.28 °C). Stage IV chlorite's temperature varies from 174.1 to 192.6 °C (average of 184.4 ± 4.09 °C), showing a similar temperature to stage III. The inconsistency of the temperature and the Fe-Mg ratio is because of the difference occurring in the tetrahedral Al site. Although stage III chlorite has more abundant Fe than stage IV, it has less Al in the tetrahedral site (Table 3). This resulted in the similar temperature of stage III and IV chlorites. Detailed EPMA results are provided in Supplementary Table S3.

Table 3. Major element analysis data of chlorites from Sangdong W-deposit (in brief) *.

Stage	Stage II (*n* =31)			Stage III (*n* = 26)			Stage IV (*n* =40)		
	Max	**Min**	**Average**	**Max**	**Min**	**Average**	**Max**	**Min**	**Average**
Oxide composition (wt%)									
SiO_2	26.45	30.25	27.77	24.04	27.38	25.81	24.85	27.17	25.87
TiO_2	0.03	0.12	0.17	0.05	0.05	0.08	0.01	0.14	0.05
Al_2O_3	17.68	15.76	17.20	17.42	17.44	17.44	19.54	18.97	19.20
FeO	26.26	26.24	26.65	34.07	31.43	33.18	26.95	26.98	27.09
MnO	0.59	0.61	0.60	1.23	0.90	1.09	1.03	0.97	0.99
MgO	16.04	14.92	15.24	7.28	9.35	7.96	13.42	13.03	13.34
CaO	0.01	1.17	0.27	0.02	0.05	0.06	0.01	0.11	0.02
Na_2O	0.03	0.02	0.03	0.00	0.03	0.03	0.02	0.01	0.01
K_2O	0.01	0.01	0.01	0.00	0.03	0.01	0.01	0.00	0.00
Total	87.08	89.09	87.95	84.13	86.65	85.65	85.83	87.37	86.59
Number of ions based on 28 oxygen									
Si	5.67	6.30	5.89	5.64	6.05	5.87	5.45	5.81	5.61
Al_T **	2.33	1.70	2.11	2.36	1.95	2.13	2.55	2.19	2.39
Total (T)	8.00	8.00	8.00	8.00	8.00	8.00	8.00	8.00	8.00
Al_O **	2.14	2.16	2.19	2.45	2.59	2.54	2.50	2.58	2.51
Ti	0.00	0.02	0.03	0.01	0.01	0.01	0.00	0.02	0.01
Fe^{2+}	4.71	4.57	4.73	6.68	5.81	6.31	4.94	4.82	4.91
Mn	0.11	0.11	0.11	0.24	0.17	0.21	0.19	0.18	0.18
Mg	5.13	4.63	4.82	2.55	3.08	2.70	4.39	4.15	4.31
Ca	0.00	0.26	0.06	0.01	0.01	0.01	0.00	0.03	0.01
Na	0.01	0.01	0.01	0.00	0.01	0.01	0.01	0.01	0.01
K	0.00	0.00	0.00	0.00	0.01	0.00	0.00	0.00	0.00
Geothermometry calculation									
Fe/(Fe + Mg)	0.48	0.50	0.50	0.72	0.65	0.70	0.53	0.54	0.53
Al4c	1.50	1.20	1.40	1.69	1.43	1.56	1.65	1.47	1.57
T (°C)	177.01	145.10	166.70	196.91	169.91	183.21	192.56	174.12	184.37

* Detailed data are provided in Supplementary Table S3; ** Al_T and Al_O are calculated from Al composition in tetrahedral site and octahedral site, respectively.
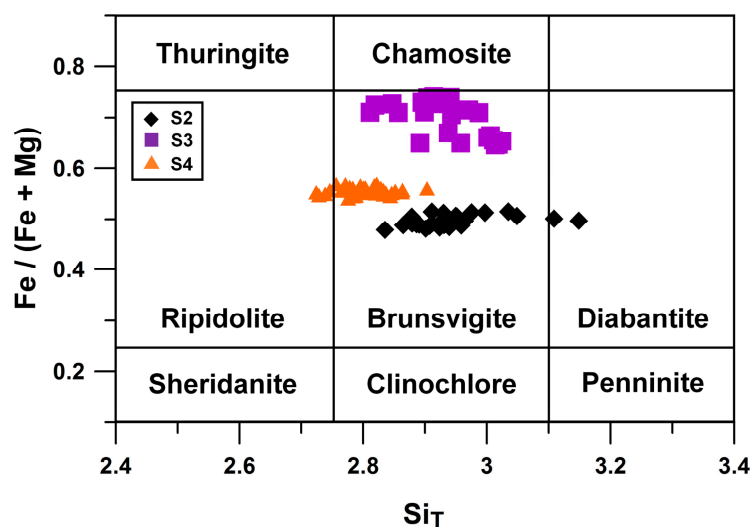
Figure 6. Chlorite classification plot of chlorites from Sangdong W-deposit. The x-axis represents the calculated Si^{4+} composition of the chlorite. The y-axis represents the ratio of Fe in chlorite. Overall composition lies in brunsvigite; few exist as ripidolite and diabantite. Each stage shows a different Fe ratio range.

5. Discussion

5.1. Textural Evidence for Sequential Scheelite Mineralization

5.1.1. Cathodoluminescence Characteristics of Scheelite

Cathodoluminescence (CL) is a common tool used to study the internal structures of scheelite [9,10,44]. The CL image of scheelite is the superimposed result of two different types of luminescence caused by distinct physical processes [45]. The self-luminescence band (SB) is a broad peak related to the molecular orbital of $[WO_4^{2-}]$ tetrahedra [46]. The maximum peak position of this SB depends on the W-Mo ratio of the scheelite, ranging from 425 (pure scheelite, blue CL color) to 530 nm (>1 wt.% Mo content, yellow CL color) [47]. Characteristic peaks (CP) are sharp peaks related to REE substitution at the Ca site of scheelite. The main peak of hydrothermal scheelite is caused by Dy^{3+} at 574 nm.

Stage I scheelite had well-developed oscillatory zoning with relatively high (up to 2.26 wt.%) Mo content (Table 1). The CL image of stage I scheelite showed no significant difference from the BSE image (Figure 3). This indicates that the SB had the most intense luminescence in the stage I scheelite, since the REE pattern of scheelite was uniform throughout the zones (Figure 5A). CL contrast differences were only observed along cracks or topographical changes. This is because CL also reflects tectonic stresses when SB is the dominant factor causing the CL contrast difference [9]. Stage II scheelite also shows similar characteristics, with similar BSE and CL images (Figure 4C,D). Stage III and IV scheelites do not show meaningful internal textures in either the BSE or CL images, only presenting slight contrast changes along subgrains or fractures (Figure 4F,G,K,L). This strongly indicates that the REE concentration of the mineralizing fluid was maintained during the mineral growth of each stage.

5.1.2. Prograde Textures of Sangdong Scheelite

The observed microtextures and mineral occurrences of stage I scheelites indicate that they have a prograde origin (Figure 3). Oscillatory zoning is the most distinguishable characteristic of stage I scheelite. Minerals with oscillatory zoning occur through various geochemical conditions, a common microtexture of solid solution minerals like scheelite and garnet [48]. The existence of oscillatory zoning in scheelite grains indicates that there were multiple fluid fluctuations or fluid infiltrations during mineral formation and suggests the possibility of dynamic changes in geochemical

conditions (i.e., oxygen (fO$_2$) or sulfur (fS$_2$) fugacity, pH, temperature, pressure, etc.) [7,13,48–50]. Oscillatory zoning of stage I scheelite shows narrow zones at the core, becoming wider towards the rim (Figure 3B,C). Unlike other internal textures of crystals (i.e., dendritic, skeletal, and cellular textures), oscillatory zoning indicates slow solidification conditions [51]. A change in zone width shows that the fluctuation period was much faster during the initial scheelite crystallization process and became relatively slower at the end. Zone width changes also appear along different directions in the same zone (Figure 3B,C). This indicates that the growth vector of the scheelite grain was nonequivalent during mineralization for each mineral plane [9].

The existence of oscillatory zoning means that scheelite and powellite composition both appear at the grains. According to previous studies, the scheelite–powellite solid solution depends on the fO$_2$ and fS$_2$ of the system [7,49]. When the system has sufficient W and Mo content, the oxygen and sulfur concentrations determine which type of complex they make. In relatively oxidized conditions, Mo favors oxide more and forms powellite (CaMoO$_4$) rather than molybdenite (MoS$_2$) [7,49]. Thus, oscillatory zoning itself reveals relatively oxidized conditions, which can be important evidence of the prograde origin [36].

Fluid fluctuation or infiltration both need additional external fluid from outside of the system, which means that stage I scheelite was formed under an open system [13,15]. This fits well with the uniform REE pattern through oscillatory zones with different W-Mo content, since an influx of external fluid will keep providing REE to the mineralizing fluid (Figure 5A). Through this evidence, the reason that scheelite with oscillatory zoning commonly shows relatively larger grain sizes also can be explained, since grain size is related to pore space, growth velocity, and fluid composition [52]. Stage I scheelite was formed slowly in the large pore space of veinlets, under continuous fluid influx and fluctuations in the open system at the late prograde stage.

5.1.3. Retrograde Textures of Sangdong Scheelite

Stage II scheelite also has oscillatory zoning but overall sizes are much smaller than stage I scheelite (Figure 4A–D). A significant feature of oscillatory zoning of stage II scheelite is dented zones (Figure 4C,D). Unlike straight zones of stage I scheelite, zones of stage II scheelite are dented and folded. This can be meaningful evidence of the pressure release of the fluid. At the end of the prograde stage, magmatic–hydrothermal fluid loses its initial pressure and ceases rising from the magmatic body, forming a stock [36]. This results in regional metamorphism around the stock, which slowly cools from the outer boundary of the stock during the retrograde stage. As the outer shell becomes harder and thicker, incompatible volatiles are released into the hollow and start to build pressure [52]. When the internal pressure becomes high enough to break the walls and fracture the surrounding formation, it forms secondary veins at the system. When mineral crystals are formed under these conditions, zoning can be dented through the effect of high pressure [48]. This explains that the dented zones of stage II scheelite resulted from pressure release during the early retrograde stage.

The predominance of scheelite among the vein-forming minerals also can be evidence of the early retrograde stage. Unlike stage III and IV scheelites, quartz grains are hard to find at the stage II veins (Figure 4A,B). Scheelite constitutes most of the vein spaces, which means that the mineralizing fluid was abundant with Ca and W. Since the main elements (Ca, W) are gradually consumed as mineralization proceeds, scheelite abundance also decreases as precipitation continues. Thus, the abundant scheelite content of stage II veins indicates that they are formed at a relatively earlier period of the retrograde stage than stage III and IV scheelites. Abundant hydrous secondary minerals (chlorite, ferro-actinolite) and minor amounts of sulfide mineral (pyrrhotite) also fit well with its retrograde origin [36].

Stage III scheelite does not show any internal zoning textures in either the BSE or CL images (Figure 4E–G). Grains were commonly elongated along the vein directions. Sharp margins with quartz grains indicate that they were formed at similar periods; dissolved boundaries with chlorites indicate that chlorite was formed later than the scheelite grains. Almost pure stage III scheelite strongly indicates its retrograde origin. The retrograde stage generally shows lower fO$_2$ and higher fS$_2$ values

than the prograde stage [36]. This geochemical condition favors scheelite over powellite, as Mo preferentially forms molybdenite in such environments [7,49,53]. This mechanism was commonly reported in other W-deposits [13,44,54–58]. A high fS_2 condition leads to abundant formation of sulfide minerals (pyrrhotite, bismuthinite), but the absence of sulfide minerals with higher sulfur content (i.e., pyrite, sphalerite, molybdenite) indicates that the sulfur fugacity of stage III scheelite was lower than that of stage IV scheelite. Relatively larger grain sizes and a higher scheelite content also supports the notion that stage III scheelite was formed earlier than stage IV scheelite (Figure 4E–G).

Stage IV scheelite also does not show meaningful internal microtextures in either the BSE or CL images (Figure 4K,L). Scheelite grains are smaller and disseminated with low abundancy. Sawblade-shaped authigenic chlorite and subhedral scheelite grains with quartz show a simultaneous genetic relationship (Figure 4H–L). The pure scheelite composition can be explained by the same mechanism as stage III scheelite. The biggest difference is the type of sulfide minerals and scheelite content in the vein. The existence of high sulfur content sulfides (pyrite, sphalerite) and the scarce occurrence of scheelite can be strong evidence that stage IV scheelite was formed later than stage III scheelite [36]. This fits well with the field observation that quartz veins with mica alteration crosscut quartz veins with amphibole alteration [3].

The chlorite geothermometer also can support this sequential mineralization. Chlorite mineralization along tungsten minerals is well observed as a common phenomenon in the quartz–scheelite vein system [59]. The temperature estimated by the chlorite geothermometer increases from stage II (166.7 ± 6.75 °C) to stage III (183.2 ± 8.28 °C) and stage IV (184.4 ± 4.09 °C). This temperature can provide a lower boundary of scheelite formation at each stage [59]. A slight increase in temperature might be related to the distance from the magma body and the geothermal gradient. A previous fluid inclusion study of quartz grains from stage III and IV veins suggested the formation temperature of each stage as 280 to 300 °C (1–3 km, 0.3–0.9 kbar) and 320 to 340 °C (5–6 km, 1.3–1.7 kbar) [3]. This result supports different stages of scheelite formation between hanging wall, main, and footwall orebodies. Thus, for the reasons discussed above, scheelites found in quartz veins of the Sangdong W-deposit show clear textural evidence of sequential mineralization consisting of at least four stages. The mineral occurrence for each stage is provided in Table 4.

Table 4. Summarized table of mineralogical occurrence of each quartz–scheelite vein stage.

Characteristics	Late Prograde Stage	Retrograde Stage		
	Stage I	Stage II	Stage III	Stage IV
Orebody Type (Location)	Quartz vein (Hanging wall)	Scheelite vein (Hanging wall)	Quartz vein (Middle, main)	Quartz–Stilbite vein (Footwall)
Mineral assemblage associated with scheelite	Quartz, Fluorite, Apatite	Fluorite, Chlorite, Calcite, Apatite, Quartz	Quartz, Chlorite, Pyrrhotite, Fluorite, Apatite, Native Bismuth, Bismuthinite	Quartz, Chlorite, Biotite, Fluorite, Apatite, Pyrite, Sphalerite, Bismuthinite, Stilbite
Secondary minerals	Quartz, Biotite, Muscovite, K-feldspar, Ca-plagioclase	Ferro-actinolite, Chlorite, Calcite, Ca-plagioclase, Stilbite	Ferro-actinolite, Biotite, Quartz, K-feldspar	Quartz, Biotite, Muscovite, K-feldspar, Pyrite

5.2. Fluid Evolution and Trace Element Behavior

5.2.1. Scheelite Mineral Chemistry

Scheelite is a tetragonal mineral composed of tetrahedral $[WO_4]^{2-}$ and dodecahedral $[CaO_8]^{14-}$ [9,60,61]. REE^{3+} substitution occurs with the Ca^{2+} site, which requires a charge compensating mechanism to maintain the charge neutrality [11]. Three mechanisms are mainly suggested as exchange vectors for REE substitution [8,62,63]:

$$2Ca^{2+} = REE^{3+} + Na^+ \qquad (3)$$

$$Ca^{2+} + W^{6+} = REE^{3+} + Nb^{5+} \qquad (4)$$

$$3Ca^{2+} = 2REE^{3+} + \square \qquad (5)$$

$\square$ in Formula (5) is a vacant Ca site determined by checking the numerical relationship between REE and Na or Nb contents. If Na is the dominant exchange vector of the scheelite, the Ca site would preferentially intake REE with a similar ionic radius [8]. The Na content of Sangdong scheelites are enough to be detected during both EPMA and LA-ICP-MS (Figure 7A and Table S2). However, Na and REE concentrations (REE–Eu + Y) of scheelite at each stage are generally scattered from the 1:1 line and do not show a meaningful correlation. Irregular enrichment of Na in stage IV scheelites might originate from later sodium alteration which formed stilbite in the vein [64,65]. This suggests that Na did not play a significant role in the REE substitution of Sangdong scheelites. For the exchange vector in Equation (4), Nb^{5+} and Ta^{5+} both work on the substitution. Nb^{5+} is abundant (10.14 to 479.81 ppm) but Ta^{5+} is relatively scarce (0.102 to 8.69 ppm) in scheelite, showing no significant correlation with REE concentration (Figure 7B and Table S2). This indicates that the exchange vector of Formula (4) is also not a major REE substitution mechanism. Therefore, the exchange vector of Formula (5) with the Ca-vacant site remains as a reasonable vector. This vector increases the flexibility of the substitution sites, resulting in the inheritance of the REE pattern from the mineralizing fluid [8,9]. This makes scheelite a useful tool to trace the geochemical evolution of magmatic–hydrothermal fluid.
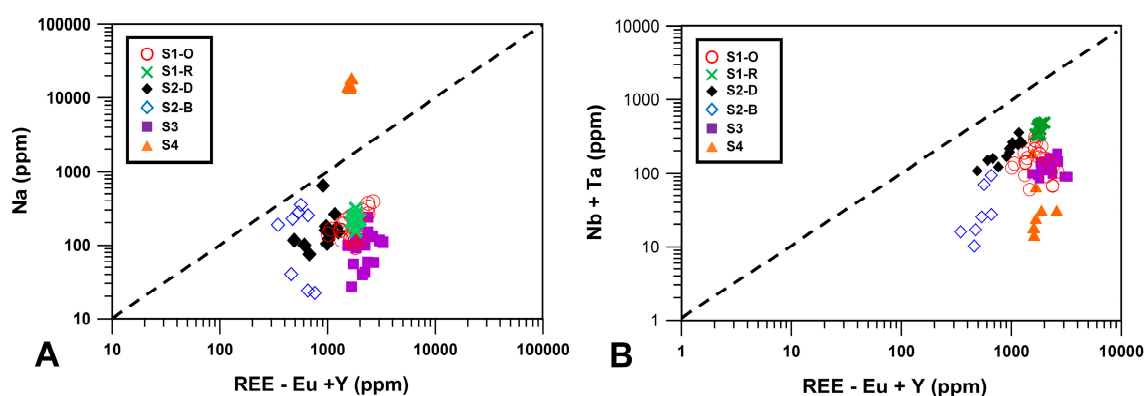

Figure 7. (**A**) Plot versus Na concentration and (REE–Eu + Y) concentration. The dashed line in the center is the ideal 1:1 correlation line. Most scheelites have a higher amount of REE than Na, which means that Na did not play significant role in the REE substitution of scheelite. Extraordinary abundance of Na in stage IV scheelite might be affected by later-stage sodium alteration, which produced stilbite in the quartz–scheelite veins of the footwall orebody. (**B**) Plot versus Nb + Ta and (REE–Eu + Y) concentration. The dashed line in the center is the ideal 1:1 correlation line. Scheelite has a higher amount of REE than Nb + Ta, which means that Nb + Ta also was not a main substitution mechanism of the deposit.

5.2.2. Rare Earth Element Characteristics

A total of 89 points of LA-ICP-MS analysis was conducted for Sangdong scheelites. Each scheelite from different stages showed distinct REE patterns and trace element characteristics. To check the REE patterns of each stage briefly, a plot of $(La/Sm)_N$ versus $(Gd/Lu)_N$ was constructed (Figure 8A). Each stage shows a slightly different trend but mostly lies on $(La/Lu)_N = 1$. Oscillatory zoning of stage I scheelites shows relatively higher $(La/Lu)_N$ values, suggesting its positively inclined LREE-enriched REE pattern (Figure 5A). The rim areas of stage I scheelites and the bright areas of stage II scheelites show relatively depleted LREE patterns (Figure 5A,B). Dark areas of stage II scheelites and stage III and IV scheelites show similar $(La/Lu)_N$ values but differing MREE concentrations and Eu anomalies (Figure 8A). The $(La/Sm)_N$ versus $(Eu/Eu^*)_N$ plot can provide information about fluid origins (Figure 8B). When minerals are precipitated from fluids with the same origin, data will be plotted on the same trend [9]. The bright area of stage II scheelite only lies on a different trend from the other samples, which could be evidence of meteoric mixing during the early retrograde stage. This can also explain the low REE concentration, resulting from dilution by meteoric water [66,67].
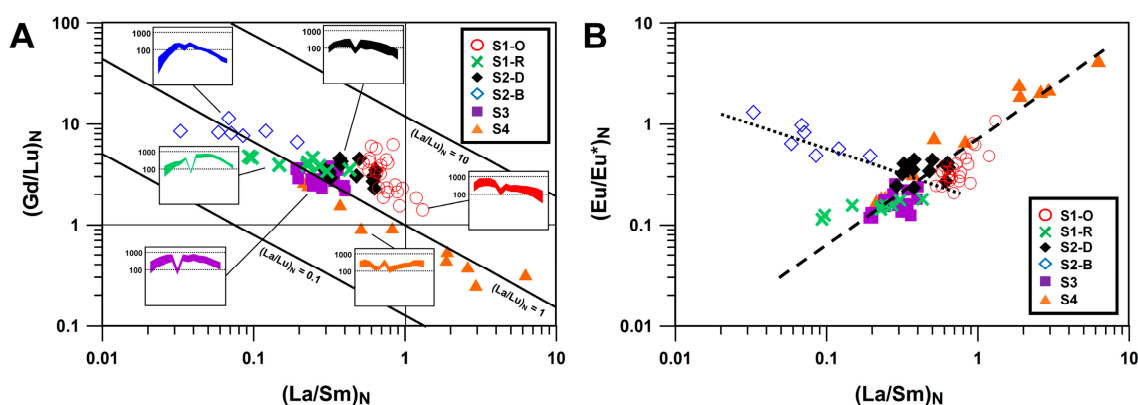

Figure 8. (**A**) Plot versus $(Gd/Lu)_N$ and $(La/Sm)_N$. Isolines of $(La/Lu)_N$ are solid lines, calculated by assuming that Sm_N and Gd_N have approximately equal values. Most scheelites are plotted along the $(La/Lu)_N = 1$ line, and S1-O plotted higher than the line represents LREE enrichment. (**B**) Plot versus $(Eu/Eu^*)_N$ and $(La/Sm)_N$. Eu^*_N is calculated as $(Sm_N \times Gd_N)^{1/2}$. Eu anomaly shows linear trend in most scheelites and only S2-B shows different trend. This indicates that Sangdong scheelites were made by a single granitic body. Low REE content and weak Eu anomaly of S2-B can be evidence of meteoric mixing at the retrograde stage.

Oscillatory zoning of stage I scheelite shows a uniform pattern despite the Mo concentration difference. In general, the partitioning of elements between fluid and minerals depends on the partitioning coefficient. The lattice strain model (LSM) explains this through the relationship between crystal lattice elasticity and ionic size [68,69]. LSM was applied to scheelite to obtain a partitioning coefficient that better fits the scheelite–hydrothermal fluid geochemistry [11]. The calculated model and empirical data showed similar LREE-enriched patterns, indicating that the REE concentration of the initial fluid affects the REE pattern of scheelite itself. According to a previous study, the granitic body beneath the Sangdong deposit (Sangdong granite) had an LREE-enriched pattern [34]. In general, granitic melt and magmatic–hydrothermal fluids show this type of REE pattern [13,66,70,71]. To check the trend of trace elements along the oscillatory zones, an element distribution plot was drawn, as shown in Figure 9.

According to Figure 9, we could check whether LREE and HREE behave similarly as groups and Y acts with a similar trend to the HREEs. This is obvious since Y^{3+} has a similar ionic radius (104 Å) to HREEs (102 Å in average) than LREEs (113.46 Å) or Eu (108.7 Å). Eu acts independently, showing no correlation with any other element. This fits well with the characteristics of Eu, which is generally affected by redox conditions or the system itself [9,12,44]. Sr shows a negative correlation with Mo

content, which fits well with the observations of previous researchers [72]. This might be caused by changes in fluid–rock interaction ratios. Elements which can participate at the REE exchange vector (Na, Nb, and Ta) do not show a meaningful correlation with other REEs. This fits well with previous explanations of the Ca-vacancy substitution.
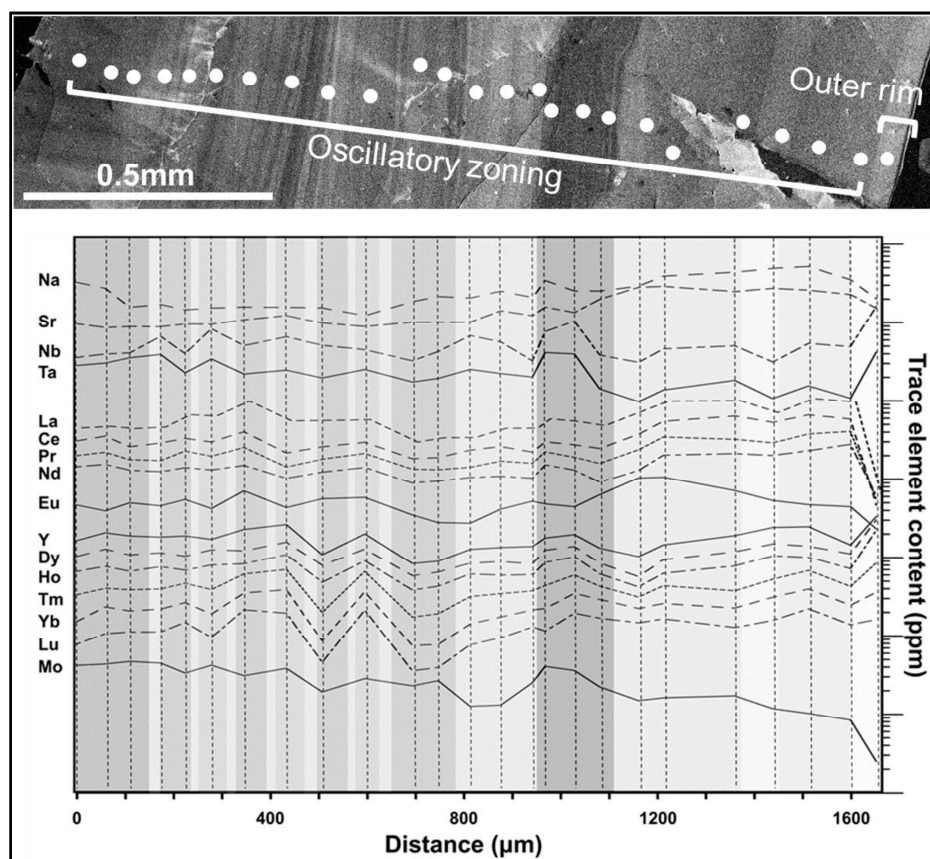

Figure 9. Element trend plot along the oscillatory zones of stage I scheelite. Concentrations of each trace element are plotted with realistic scale. This graph provides information about behavior characteristics of each trace element.

The rim area of stage I scheelite shows a strong depletion of LREE and relatively enriched MREE (Figure 5A). Despite the difference in REE profile with the oscillatory zoned area, sharp and straight boundaries indicate that the rim area did not originate from a different stage [52]. This can be explained by the mineralization environment of stage I scheelite. As explained previously, stage I scheelite was formed slowly during the late prograde stage. Continuous fluid infiltration and fluctuation caused a uniform REE profile through the oscillatory zoning formation sequence. As we can see in Figure 3C, the thickness of zones became relatively larger from the core to the rim. This indicates that the fluid influx frequency decreased, and fluid composition was maintained for a relatively longer period. We also can demonstrate that the rim area of stage I scheelite is much thinner than other oscillatory zoning parts (Figure 3B,C). Thus, when the rim areas were precipitated, LREE was highly consumed by previously formed oscillatory zoned parts, resulting in LREE depletion. The short mineralization period and relatively smaller volume of the rim area probably caused the relative enrichment of MREE and HREE.

Significant characteristics of REE profiles from retrograde scheelites are changes in MREE concentration and Eu anomaly. Stage II and III scheelites have MREE-enriched M-type tetrad shapes (Figure 5B,C), shifting to an MREE-depleted W-type tetrad shape (Figure 5D). This REE profile change can be strong evidence of fractional crystallization of REE by scheelite [9,73]. If the initial mineralizing

fluid is the MREE-enriched type, MREE becomes depleted as mineralization progresses. Precipitation of scheelite itself works as an MREE scavenger of the system, and the co-precipitation of MREE-favorable minerals (i.e., fluorapatite) can also affect the MREE fractionation of the system [9]. The MREE enriched fluid pattern of the initial fluid can be caused by constant LREE consumption through stage I scheelite formation. This REE differentiation mechanism was generally studied through single grains with different zones, estimating that the grain underwent several stages of MREE depletion [8,9]. It is important that this fractional crystallization mechanism in the closed system is proven through sequential scheelite formation in the quartz–scheelite vein system of the Sangdong W-deposit.

5.2.3. Eu Anomalies and Fractional Crystallization

Eu anomalies are important factors for tracking the geochemical environment of the deposit [9,12,13,44,74,75]. Dominant factors that cause Eu anomaly are changes in the redox conditions of the system. In Figure 10A, data points are mostly plotted at the range of $0.1 \leq \delta Eu [(Eu/Eu^*)_N] \leq 1$, suggesting that Eu is dominated by Eu^{3+}. This fits well with the dominant negative Eu anomalies of the deposit. Only stage IV scheelite with positive Eu anomalies exists above the $\delta Eu = 1$ line, indicating the dominance of Eu^{2+}. Since Eu^{2+} fits better with the Ca site than Eu^{3+}, a positive Eu anomaly appears in the scheelite when the system has sufficient Eu^{2+} [8]. Eu anomaly can be affected by four main factors: (1) coexisting minerals [76]; (2) redox condition [77]; (3) parental hydrothermal fluid composition [78], and (4) fractional crystallization [9,44].
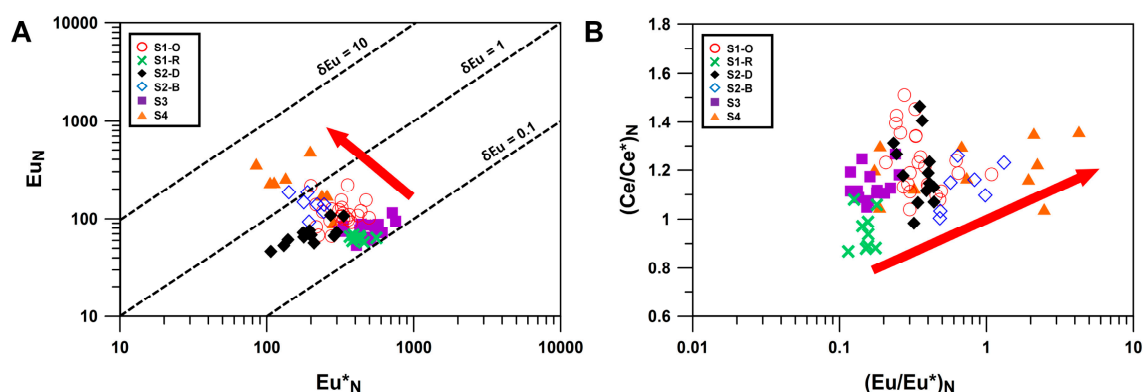

Figure 10. (**A**) Plot of chondrite normalized Eu concentrations (Eu_N) versus calculated Eu^*_N. Dashed lines represent δEu (Eu_N/Eu^*_N) isolines for 0.1, 1, and 10. Increasing δEu value means predominance of Eu^{2+}, shifting into positive Eu anomaly. (**B**) Plot of δEu versus δCe (Ce_N/Ce^*_N), when Ce^*_N is value of $(La_N \times Pr_N)^{1/2}$. δCe roughly increases as δEu increases from earlier stage to later stage. Increasing Ce anomaly indicates that the system changed into a more reduced environment.

Firstly, scheelite can compete with the coexisting minerals to scavenge REE from the fluid. Generally, prograde skarn minerals with high Ca compositions (i.e., clinopyroxene, garnet) can hold abundant REE content [10]. Quartz–scheelite veins of the Sangdong W-deposit do not contain high amounts of calcic minerals except scheelite, and common Ca-accessory minerals (fluorite, apatite) do not hold large amounts of REE.

The redox condition seems to have a meaningful effect on Eu anomalies [10]. Since Mo forms Mo^{6+} at relatively oxidized conditions, powellite composition can be a useful indicator of redox condition estimation [79]. To compare, the powellite content of the Sangdong W-deposit is relatively lower than the Kara W-deposit [80], the Jitoushan and Baizhangyan W–Mo deposit [10], or the Weondong W–deposit [13]. This indicates that the quartz–scheelite veins of Sangdong W-deposit were formed under relatively reduced conditions. Similar to Eu, the Ce anomaly also can be a useful tool to estimate the redox condition (Figure 10B). Ce forms Ce^{4+} at oxidized conditions and Ce^{3+} at reduced conditions. Since Ce^{3+} favors the Ca site, a roughly positive correlation between $\delta Ce [(Ce/Ce^*)_N]$ and δEu provides

evidence of reduced conditions. This could be one of the reasons for the increasing Eu anomaly in stage IV scheelite.

Another possible explanation of the Eu anomaly is the fluid composition itself. The Sangdong W-deposit is known to be formed from hidden Sangdong granite. The REE profile of this granite was a positively inclined, LREE-enriched pattern with a negative Eu anomaly [34]. This can explain the negative Eu anomaly of stage I scheelite. Scheelites of stages II to IV are also from the same fluid origin, so this can be a reasonable factor for the negative Eu anomaly of the retrograde stage also.

Fractional crystallization is the most important factor that can affect the Eu anomaly of the system. The partition coefficient of Eu not only depends on the mineral chemistry and substitution elements but also on fluid composition [9]. Eu^{2+} and Eu^{3+} have different partition coefficients in the system, and the contrast between the two partition coefficients changes through fractional crystallization. Fluid composition affects Eu^{3+} rather than Eu^{2+}, and the difference becomes stronger as fractional crystallization progresses [9]. This can provide good evidence of the change from the slightly negative Eu anomaly of stage II scheelite to the positive Eu anomaly of stage IV scheelite. Therefore, of all the factors that can provide explanations of the Eu anomalies, fractional crystallization seems to provide the most useful and clear explanation.

5.3. Scheelite Mineralization Model of Sangdong W-Deposit

Through the microtextural and geochemical evidence from scheelites, we have discussed the sequential mineralization of scheelite from the quartz–scheelite vein system. A schematic figure of scheelite mineralization is suggested in Figure 11.

Magmatic–hydrothermal fluid released from the granitic body rises through the Myobong slate formation, forming large-scale prograde skarn zones. Fluid gradually loses initial pressure and cumulates at the boundary of the Pungchon limestone formation and the Myobong slate formation. Stage I scheelite forms at this stage, growing slowly with well-developed oscillatory zoning. The uniform REE profile along the oscillatory zoning indicates that stage I scheelite was formed in an open system with periodic fluid fluctuation. Internal pressure increases as the outer rim of the hollow solidifies, resulting in pressure release of retrograde hydrothermal fluid. Released fluid favorably flows back through the formally fractured path, rather than fracturing upward into the unmetamorphosed surrounding formation. This gravitational backflow is a common phenomenon which occurs in vein-type massive sulfide ores [81,82]. Stage II scheelite with abundant REE forms first at the hanging wall orebody, then stage III at the main ore body and stage IV at the footwall orebody forms last. Shifting of the REE profile from an MREE-enriched M-type tetrad pattern (negative Eu anomaly) to an MREE-depleted W-type tetrad pattern (positive Eu anomaly) reveals that the retrograde quartz–scheelite vein was formed under reduced conditions in the closed system. After W is all consumed at the footwall orebody, fluid might migrate deeper and form quartz–molybdenite veins of Jangsan quartzite, at highly reduced conditions. This model also agrees with previous age data of the main orebody (87.2 Ma) and footwall orebody (86.6 Ma) [3].
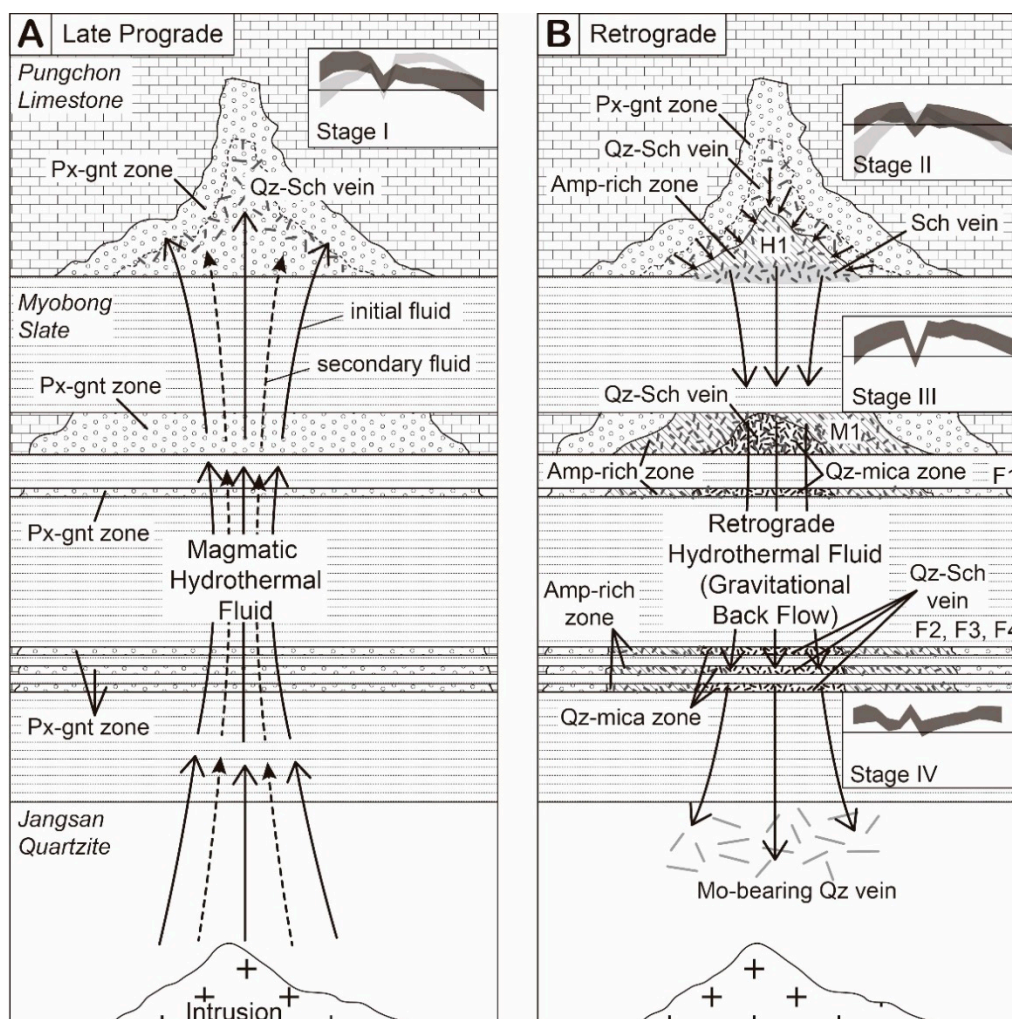
Figure 11. Schematic diagram of scheelite mineralization at the quartz–scheelite vein system of the Sangdong W-deposit. (**A**) Initial magmatic–hydrothermal fluid releases from the granitic body and forms prograde skarn. Secondary fluid of the late prograde stage forms magmatic stock, slowly filling the fractures, and forms stage I scheelite of quartz–scheelite veins. (**B**) Retrograde hydrothermal fluid migrates through pressure release and gravitational back flow mechanism through fractures. As W in the mineralizing fluid is consumed gradually, stage II to IV scheelites form through fractional crystallization. Final stage of reduced condition and W-poor fluid forms quartz–molybdenite vein of Jangsan quartzite formation.

6. Conclusions

(1) The quartz–scheelite vein system of the Sangdong W-deposit shows sequential scheelite formation from the late prograde stage (magmatic–hydrothermal fluid from granitic body) to the overall retrograde stage (hydrothermal fluid from pressure release).

(2) Clear and straight oscillatory zoning and large grain size of stage I scheelite indicate slow crystal growth and periodic fluid fluctuation. Uniform REE profiles along the oscillatory zones are evidence of continuous fluid influx under the open system. LREE-enriched patterns suggest the magmatic–hydrothermal fluid origin of the stage I scheelite. The REE difference in the rim area was caused by LREE consumption during slow mineral growth.

(3) Retrograde scheelites have relatively lower Mo content than stage I scheelite. Dented oscillatory zones of stage II scheelite suggest pressure release of retrograde hydrothermal fluid. Fluid migrated through fractures by pressure release and gravitational backflow from the hanging wall orebody to

the footwall orebody. MREE depletion and Eu anomaly shifting are strong evidence of systematical fractional crystallization in the closed system.

(4) The chlorite geothermometer can provide the closure temperature of veins. This can provide additional information about mineral forming stages when it is combined with fluid inclusion studies.

Supplementary Materials: The following are available online at http://www.mdpi.com/2075-163X/10/8/678/s1, Table S1: Raw data of scheelite EPMA analysis, Table S2: Raw data of scheelite LA-ICP-MS analysis, Table S3: Chlorite geothermometry calculation.

Author Contributions: Conceptualization, W.C., C.P. (Changyun Park), and Y.S.; Data curation, W.C., C.P. (Chaewon Park), H.K., and C.L.; Formal analysis, W.C., C.P. (Changyun Park), and Y.S.; Funding acquisition, Y.S.; Investigation, W.C., C.P. (Chaewon Park), H.K., and C.L.; Methodology, W.C. and Y.S.; Project administration, C.P. (Changyun Park) and Y.S.; Supervision, Y.S.; Writing—original draft, W.C.; Writing—review and editing, C.P. (Changyun Park) and Y.S. All authors have read and agreed to the published version of the manuscript.

Conflicts of Interest: The authors declare no conflict of interest.

References

1. Lee, H.J. *Report on Sangdong Tungsten Min in Korea*; Korea Enginnering Co. Ltc: Seoul, Korea, 2001.
2. John, Y.W. Geology and origin of Sangdong tungsten mine, Republic of Korea. *Econ. Geol.* **1963**, *58*, 1285–1300.
3. Seo, J.H.; Yoo, B.C.; Villa, I.M.; Lee, J.H.; Lee, T.H.; Kim, C.S.; Moon, K.J. Magmatic-hydrothermal processes in Sangdong W-Mo deposit, Korea: Study of fluid inclusions and 39Ar–40Ar geochronology. *Ore Geol. Rev.* **2017**, *91*, 316–334. [CrossRef]
4. Newberry, R.; Einaudi, M. Tectonic and geochemical setting of tungsten skarn mineralization in the Cordillera. *Ariz. Geol. Soc. Dig.* **1981**, *14*, 99–111.
5. Newberry, R.; Swanson, S. Scheelite skarn granitoids: An evaluation of the roles of magmatic source and process. *Ore Geol. Rev.* **1986**, *1*, 57–81. [CrossRef]
6. Kwak, T.; Abeysinghe, P. Rare earth and uranium minerals present as daughter crystals in fluid inclusions, Mary Kathleen U-REE skarn, Queensland, Australia. *Mineral. Mag.* **1987**, *51*, 665–670. [CrossRef]
7. Hsu, L. Effects of oxygen and sulfur fugacities on the scheelite-tungstenite and powellite-molybdenite stability relations. *Econ. Geol.* **1977**, *72*, 664–670. [CrossRef]
8. Ghaderi, M.; Palin, J.; Campbell, I.; Sylvester, P. Rare earth element systematics in scheelite from hydrothermal gold deposits in the Kalgoorlie-Norseman region, Western Australia. *Econ. Geol.* **1999**, *94*, 423–437. [CrossRef]
9. Brugger, J.; Lahaye, Y.; Costa, S.; Lambert, D.; Bateman, R. Inhomogeneous distribution of REE in scheelite and dynamics of Archaean hydrothermal systems (Mt. Charlotte and Drysdale gold deposits, Western Australia). *Contrib. Mineral. Petrol.* **2000**, *139*, 251–264. [CrossRef]
10. Sun, K.; Chen, B.; Deng, J. Ore genesis of the Zhuxi supergiant W-Cu skarn polymetallic deposit, South China: Evidence from scheelite geochemistry. *Ore Geol. Rev.* **2019**, *107*, 14–29. [CrossRef]
11. Zhao, W.; Zhou, M.; Williams-Jones, A.; Zhao, Z. Constraints on the uptake of REE by scheelite in the Baoshan tungsten skarn deposit, South China. *Chem. Geol.* **2018**, *477*, 123–136. [CrossRef]
12. Wu, S.; Mao, J.; Ireland, T.R.; Zhao, Z.; Yao, F.; Yang, Y.; Sun, W. Comparative geochemical study of scheelite from the Shizhuyuan and Xianglushan tungsten skarn deposits, South China: Implications for scheelite mineralization. *Ore Geol. Rev.* **2019**, *109*, 448–464. [CrossRef]
13. Choi, W.; Park, C.; Song, Y. Multistage W-mineralization and magmatic-hydrothermal fluid evolution: Microtextural and geochemical footprints in scheelite from the Weondong W-skarn deposit, South Korea. *Ore Geol. Rev.* **2020**, *116*, 103219. [CrossRef]
14. Pak, S.; Choi, S.; Choi, S. Systematic mineralogy and chemistry of gold-silver vein deposits in the Taebaeksan district, Korea: Distal relatives of a porphyry system. *Mineral. Mag.* **2004**, *68*, 467–487. [CrossRef]
15. Park, C.; Choi, W.; Kim, H.; Park, M.; Kang, I.; Lee, H.; Song, Y. Oscillatory zoning in skarn garnet: Implications for tungsten ore exploration. *Ore Geol. Rev.* **2017**, *89*, 1006–1018. [CrossRef]

16. Kim, K.H.; Kim, O.J.; Nakai, N.; Lee, H.J. Stable isotope studies of the Sangdong tungsten ore deposits, South Korea. *Min. Geol.* **1988**, *38*, 473–487.

17. Park, H.-I.; Chang, H.W.; Jin, M.S. K-Ar ages of mineral deposits in the Taebaeg Mountain district. *Econ. Environ. Geol.* **1988**, *21*, 57–67.

18. Choi, S.; Pak, S. The Origin and Evolution of the Mesozoic Ore-forming Fluids in South Korea: Their Genetic Implications. *Econ. Environ. Geol.* **2007**, *40*, 517–535.

19. Chang, H.; Lee, M.; Park, H.; Kim, J.; Chi, J. Study of the Taebaeksan mineralized Area. *Kosef Report.* **1990**, 173–264.

20. Chang, K.; Woo, B.; Lee, J.; Park, S.; Yao, A. Cretaceous and Early Cenozoic Stratigraphy and History of Eastern Kyŏngsang Basin, S. Korea. *J. Geol. Soc. Korea* **1990**, *26*, 471–487.

21. Jin, M.; Kim, S.; Seo, H.; Kim, S. *K-Ar Fission Track Dating for Granites and Volcanic Rocks in the Southeastern Part of Korean Peninsula*; Korea Institute of Energy and Resources: Daejeon, Korea, 1989.

22. Kim, O. Metallogenic epochs and provinces of South Korea. *J. Geol. Soc. Korea* **1971**, *7*, 37–59.

23. Shelton, K.L.; So, C.-S.; Chang, J.-S. Gold-rich mesothermal vein deposits of the Republic of Korea; geochemical studies of the Jungwon gold area. *Econ. Geol.* **1988**, *83*, 1221–1237. [CrossRef]

24. Cluzel, D.; Jolivet, L.; Cadet, J. Early middle Paleozoic intraplate orogeny in the Ogcheon belt (South Korea): A new insight on the Paleozoic buildup of East Asia. *Tectonics* **1991**, *10*, 1130–1151. [CrossRef]

25. Choi, S.; Ryu, I.; Pak, S.; Wee, S.; Kim, C.; Park, M. Cretaceous epithermal gold-silver mineralization and geodynamic environment, Korea. *Ore Geol. Rev.* **2005**, *26*, 115–135. [CrossRef]

26. Cho, D.; Kwon, S. Hornblende geobarometry of the Mesozoic granitoids in South Korea and the evolution of the crustal thickness. *J. Geol. Soc. Korea* **1994**, *30*, 41–61.

27. Hong, S.; Cho, D. *Late Mesozoic-Cenozoic Tectonic Evolution of Korea (3)*; KR-03-01; KIGAM: Daejeon, Korea, 2003; pp. 455–526.

28. Moon, K.J. The Genesis of the Sangdong Tungsten Deposit, the Republic of Korea. Ph.D. Thesis, University of Tasmania, Hobart, Australia, 1983; p. 153, Unpublished.

29. Hedenquist, J.W.; Lowenstern, J.B. The role of magmas in the formation of hydrothermal ore deposits. *Nature* **1994**, *370*, 519–527. [CrossRef]

30. Hwang, D.; Lee, J. Ore genesis of the Wondong polymetallic mineral deposits in the Taebaegsan metallogenic province. *Econ. Environ. Geol.* **1998**, *31*, 375–388.

31. Kim, K.H. Petrology and Petrochemistry of Sangdong Granite. Master's Thesis, Kyungbuk National University, Daegu, Korea, 1986; p. 80, Unpublished.

32. Klepper, M.R. The Sangdong tungsten deposit, Southern Korea. *Econ. Geol.* **1947**, *42*, 465–477. [CrossRef]

33. Moon, K.J. Comparison study of geochemistry of the Sangdong skarn orebody in a large scale and small scale. *Econ. Environ. Geol.* **1986**, *19*, 113–119.

34. Moon, K.J. REE patterns at the Sangdong tungsten skarn ore deposit. South Korea. *J. Geol. Soc. Korea.* **1989**, *25*, 205–215.

35. Pearce, N.; Perkins, W.; Westgate, J.; Gorton, M.; Jackson, S.; Neal, C.; Chenery, S. A compilation of new and published major and trace element data for NIST SRM 610 and NIST SRM 612 glass reference materials. *Geostand. Newsl.* **1997**, *21*, 115–144. [CrossRef]

36. Meinert, L. Skarns and skarn deposits. *Geosci. Can.* **1992**, *19*, 145–162.

37. Hayes, J.B. Polytypism of chlorite in sedimentary rocks. *Clays Clay Miner.* **1970**, *18*, 285–306. [CrossRef]

38. Kranidiotis, P.; MacLean, W. Systematics of chlorite alteration at the Phelps Dodge massive sulfide deposit, Matagami, Quebec. *Econ. Geol.* **1987**, *82*, 1898–1911. [CrossRef]

39. Cathelineau, M. Cation site occupancy in chlorites and illites as a function of temperature. *Clay Miner.* **1988**, *23*, 471–485. [CrossRef]

40. Jowett, E. Fitting iron and magnesium into the hydrothermal chlorite geothermometer. In Proceedings of the GAC/MAC/SEG Joint Annual Meeting, Toronto, ON, Canada, 27–29 May 1991. Program with Abstracts 16.

41. Vidal, O.; Parra, T.; Vieillard, P. Thermodynamic properties of the Tschermak solid solution in Fe-chlorite: Application to natural examples and possible role of oxidation. *Am. Mineral.* **2005**, *90*, 347–358. [CrossRef]

42. Bourdelle, F.; Parra, T.; Chopin, C.; Beyssac, O. A new chlorite geothermometer for diagenetic to low-grade metamorphic conditions. *Contrib. Mineral. Petrol.* **2013**, *165*, 723–735. [CrossRef]

43. Kim, H.; Park, C.; Park, M.-H.; Song, Y. Diagenetic study on the Neogene sedimentary basin as paleoenvironmental proxy data for an offshore CO2 storage project in Pohang Basin, South Korea. *Mar. Geol.* **2019**, *416*, 105977. [CrossRef]

44. Xu, J.; Ciobanu, C.L.; Cook, N.J.; Slattery, A. Crystals from the Powellite-Scheelite series at the nanoscale: A case study from the Zhibula Cu Skarn, Gangdese Belt, Tibet. *Minerals* **2019**, *9*, 340. [CrossRef]

45. Uspensky, E.; Brugger, J.; Graeser, S. REE geochemistry systematics of scheelite from the Alps using luminescence spectroscopy: From global regularities to local control. *Schweiz. Mineral. Und Petrogr. Mitt.* **1998**, *78*, 31–54.

46. Grasser, R.; Scharmann, A. Luminescent sites in CaWO4 and CaWO4: Pb crystals. *J. Lumin.* **1976**, *12*, 473–478. [CrossRef]

47. Tyson, R.M.; Hemphill, W.R.; Theisen, A.F. Effect of the W: Mo ratio on the shift of excitation and emission spectra in the scheelite-powellite series. *Am. Mineral.* **1988**, *73*, 1145–1154.

48. Yardley, B.; Rochelle, C.; Barnicoat, A.; Lloyd, G. Oscillatory zoning in metamorphic minerals: An indicator of infiltration metasomatism. *Mineral. Mag.* **1991**, *55*, 357–365. [CrossRef]

49. Hsu, L.; Galli, P. Origin of the scheelite-powellite series of minerals. *Econ. Geol.* **1973**, *68*, 681–696. [CrossRef]

50. Shore, M.; Fowler, A. Oscillatory zoning in minerals; a common phenomenon. *Can. Mineral.* **1996**, *34*, 1111–1126.

51. L'Heureux, I. Oscillatory zoning in crystal growth: A constitutional undercooling mechanism. *Phys. Rev. E* **1993**, *48*, 4460. [CrossRef] [PubMed]

52. Hibbard, M.J. *Petrography to Petrogenesis*; Prentice Hall: Upper Saddle River, NJ, USA, 1995.

53. Einaudi, M. Skarn deposits. *Econ. Geol.* **1981**, *75*, 317–391.

54. Krauskopf, K. *Tungsten Deposits of Madera, Fresno, and Tulare Counties, California, 35*; California Division of Mines: Sacramento, CA, USA, 1953.

55. Bateman, P.; Wright, L. *Economic Geology of the Bishop Tungsten District, California*; California Division of Mines: Sacramento, CA, USA, 1956.

56. Dick, L.; Hodgson, C. The MacTung W-Cu (Zn) contact metasomatic and related deposits of the northeastern Canadian Cordillera. *Econ. Geol.* **1982**, *77*, 845–867. [CrossRef]

57. Gibert, F.; Moine, B.; Schott, J.; Dandurand, J. Modeling of the transport and deposition of tungsten in the scheelite-bearing calc-silicate gneisses of the Montagne Noire, France. *Contrib. Mineral. Petrol.* **1992**, *112*, 371–384. [CrossRef]

58. Wood, S.; Samson, I. The hydrothermal geochemistry of tungsten in granitoid environments: I. Relative solubilities of ferberite and scheelite as a function of T, P, pH, and m NaCl. *Econ. Geol.* **2020**, *95*, 143–182. [CrossRef]

59. Bobos, I.; Noronha, F.; Mateus, A. Fe-, Fe, Mn-and Fe, Mg-chlorite: A genetic linkage to W, (Cu, Mo) mineralization in the magmatic-hydrothermal system at Borralha, northern Portugal. *Mineral. Mag.* **2018**, *82*, S259–S279. [CrossRef]

60. Cottrant, J. Cristallochimie et Géochimie des Terres Rares Dans la Scheelite. Application à Quelques Gisements Français. Ph.D. Thesis, University of Paris-VI, Paris, France, 1981.

61. Brugger, J.; Giere, R.; Grobeéty, B.; Uspensky, E. Scheelite-powellite and paraniite-(Y) from the Fe-Mn deposit at Fianel, Eastern Swiss Alps. *Am. Mineral.* **1998**, *83*, 1100–1110. [CrossRef]

62. Burt, D. Compositional and phase relations among rare earth element minerals. *Rev. Mineral.* **1989**, *21*, 260–307.

63. Nassau, K.; Loiacono, G. Calcium tungstate-III: Trivalent rare earth substitution. *J. Phys. Chem. Solids* **1963**, *24*, 1503–1510. [CrossRef]

64. Hall, D.L.; Cohen, L.H.; Schiffman, P. Hydrothermal alteration associated with the iron hat iron skarn deposit, eastern Mojave Desert, San Bernardino County, California. *Econ. Geol.* **1988**, *83*, 568–587. [CrossRef]

65. Utada, M. Zeolites in hydrothermally altered rocks. *Rev. Mineral. Geochem.* **2001**, *45*, 305–322. [CrossRef]

66. Michard, A. Rare earth element systematics in hydrothermal fluids. *Geochim. Cosmochim. Acta* **1989**, *53*, 745–750. [CrossRef]

67. Audetat, A.; Gunther, D.; Heinrich, C. Causes for large-scale metal zonation around mineralized plutons: Fluid inclusion LA-ICP-MS evidence from the Mole Granite, Australia. *Econ. Geol.* **2000**, *95*, 1563–1581. [CrossRef]

68. Brice, J. Some thermodynamic aspects of the growth of strained crystals. *J. Cryst. Growth* **1975**, *28*, 249–253. [CrossRef]

69. Blundy, J.; Wood, B. Prediction of crystal-melt partition coefficients from elastic moduli. *Nature* **1994**, *372*, 452. [CrossRef]

70. Banks, D.; Yardley, B.; Campbell, A.; Jarvis, K. REE composition of an aqueous magmatic fluid: A fluid inclusion study from the Capitan Pluton, New Mexico, USA. *Chem. Geol.* **1994**, *113*, 259–272. [CrossRef]

71. Reed, M.; Candela, P.; Piccoli, P. The distribution of rare earth elements between monzogranitic melt and the aqueous volatile phase in experimental investigations at 800 °C and 200 MPa. *Contrib. Mineral. Petrol* **2000**, *140*, 251–262. [CrossRef]

72. Seo, J.H.; Yoo, B.C.; Yang, Y.S.; Lee, J.H.; Jang, J.H.; Shin, D.B. Scheelite geochemistry of the Sangdong W-Mo deposit and W prospects in the southern Taebaeksan metallo-genic region, Korea. *Geosci. J.* **2020**, *24*. [CrossRef]

73. Robb, L. *Introduction to Ore-Forming Processes*; Blackwell publishing: Hoboken, NJ, USA, 2004.

74. Sverjensky, D. Europium redox equilibria in aqueous solution. *Earth Planet. Sci. Lett.* **1984**, *67*, 70–78. [CrossRef]

75. Bau, M. Rare-earth element mobility during hydrothermal and metamorphic fluid-rock interaction and the significance of the oxidation state of europium. *Chem. Geol.* **1991**, *93*, 219–230. [CrossRef]

76. Raith, J.G.; Riemer, N.; Meisel, T. Boron metasomatism and behaviour of rare earth elements during formation of tourmaline rocks in the eastern Arunta Inlier, central Australia. *Contrib. Mineral. Petrol.* **2004**, *147*, 91–109. [CrossRef]

77. Pettke, T.; Audétat, A.; Schaltegger, U.; Heinrich, C.A. Magmatic-to-hydrothermal crystallization in the W-Sn mineralized Mole Granite (NSW, Australia): Part II: Evolving zircon and thorite trace element chemistry. *Chem. Geol.* **2005**, *220*, 191–213. [CrossRef]

78. Jiang, S.-Y.; Yu, J.-M.; Lu, J.-J. Trace and rare-earth element geochemistry in tourmaline and cassiterite from the Yunlong tin deposit, Yunnan, China: Implication for migmatitic-hydrothermal fluid evolution and ore genesis. *Chem. Geol.* **2004**, *209*, 193–213. [CrossRef]

79. Raimbault, L.; Baumer, A.; Dubru, M.; Benkerrou, C.; Croze, V.; Zahm, A. REE fractionation between scheelite and apatite in hydrothermal conditions. *Am. Mineral.* **1993**, *78*, 1275–1285.

80. Zaw, K.; Singoyi, B. Formation of Magnetite-Scheelite Skarn Mineralization at Kara, Northwestern Tasmania: Evidence from Mineral Chemistry and Stable Isotopes. *Econ. Geol.* **2000**, *95*, 1215–1230. [CrossRef]

81. Lightfoot, P.C.; Farrow, C.E. Geology, geochemistry, and mineralogy of the Worthington offset dike: A genetic model for offset dike mineralization in the Sudbury Igneous Complex. *Econ. Geol.* **2002**, *97*, 1419–1446. [CrossRef]

82. Lightfoot, P.; Zotov, I. Geology and geochemistry of the Sudbury Igneous Complex, Ontario, Canada: Origin of nickel sulfide mineralization associated with an impact-generated melt sheet. *Geol. Ore Depos.* **2005**, *47*, 349.